

## Versatile, Multivalent Nanobody Cocktails for Highly Efficient SARS-CoV-2 Neutralization

Yufei Xiang<sup>1</sup>, Shamkumar Nambulli #<sup>2</sup>, Zhengyun Xiao #<sup>1</sup>, Heng Liu #<sup>4</sup>, Zhe Sang<sup>1,3</sup>, Paul Duprex<sup>2</sup>, Dina Schneidman-Duhovny<sup>5</sup>, Cheng Zhang<sup>4</sup>, and Yi Shi<sup>1,3</sup>

1. Department of Cell Biology
2. Center for Vaccine Research
3. Pitt/CMU Program for Computational Biology
4. Department of Pharmacology and Chemical Biology  
University of Pittsburgh, Pittsburgh, PA, USA
5. School of Computer Science and Engineering, Institute of Life Sciences, The Hebrew University of Jerusalem, Israel

# Equal contributions

Correspondence: Dina Schneidman-Duhovny, Cheng Zhang or Yi Shi

### Abstract

The outbreak of COVID-19 has severely impacted global health and economy. Cost-effective therapeutics are urgently needed. Here, we used camelid immunization and proteomics to identify a large repertoire of highly potent neutralizing nanobodies (Nbs) to the SARS-CoV-2 spike protein receptor-binding domain (RBD). We discovered multiple elite Nbs of picomolar to femtomolar affinities that inhibit viral infection at as low as sub-ng/ml concentration, more potent than some of the best human neutralizing antibodies. We then determined a crystal structure of such an elite neutralizing Nb in complex with RBD. Structural proteomics and integrative modeling revealed multiple distinct and non-overlapping epitopes and indicated an array of potential neutralization mechanisms. Structural characterization facilitated the bioengineering of novel multivalent Nb constructs into multi-epitope cocktails that achieved ultrahigh neutralization potency (IC50s as low as 0.058 ng/ml) and may prevent mutational escape. Our Nbs can be rapidly produced in bulk from microbes and resist heat, lyophilization, and aerosolization. These highly promising agents are readily translated into efficient, economic, and convenient therapeutics to help end this once-in-a-century health crisis.

### Introduction

By Aug 10, 2020, a novel, highly transmissible coronavirus SARS-CoV-2 (severe acute respiratory syndrome coronavirus 2) (1, 2) has infected more than 20 million people and has claimed over 700,000 lives, with the numbers still rising. Despite preventive measures, such as quarantines and lock-downs that help curb viral transmission, the virus rebounds after lifting social restrictions. Safe and effective therapeutics and vaccines remain in dire need.

Like other zoonotic coronaviruses, SARS-CoV-2 produces the surface spike glycoprotein (S), which consists of S1 and S2 subunits forming the homotrimeric viral spike to interact with host cells. The interaction is mediated by the S1 receptor-binding domain (RBD), which binds the peptidase domain (PD) of angiotensin-converting enzyme-2 (hACE2) as a host receptor (3). Structural studies have revealed different conformations of the spike (4, 5). In the pre-fusion stage, the RBD switches between an inactive, closed conformation, and an active open conformation necessary for interacting with hACE2. In the post-fusion stage, S1 dissociates from the trimer, while S2 undergoes a dramatic conformational change to trigger host membrane fusion (6). Most recently, investigations into COVID-19 convalescence individuals' sera have led to the identifications of highly potent neutralizing IgG antibodies (NAbs) primarily targeting the RBD but also non-RBD epitopes (7-13). High-quality NAbs may overcome the risks of the Fc-associated antibody-dependent enhancement (ADE) and are promising therapeutic and prophylactic candidates (14, 15).

The  $V_{HH}$  antibodies or nanobodies (Nbs) are minimal, monomeric antigen-binding domains derived from camelid single-chain antibodies (16). Unlike IgG antibodies, Nbs are characterized by small sizes (~15 kDa), high solubility and stability, ease of bioengineering into bi/multivalent forms, and low-cost efficient microbial productions. Because of the robust physicochemical properties, Nbs are flexible for administration, including inhalation, making their use against the respiratory, viral targets appealing (17, 18). Previous efforts have yielded broadly neutralizing Nbs for various challenging viruses, including Dengue, RSV, and HIV (17, 19, 20). Very recently, several SARS-CoV-2 neutralizing Nbs have been identified, by screening SARS-CoV or MERS cross-reacting Nbs or using synthetic Nb libraries for RBD binding. However, these synthetic Nbs generally neutralize the virus at  $\mu\text{g}$  to sub- $\mu\text{g}/\text{ml}$  concentration (12, 21-25), which are hundreds of times less potent than the best NAbs, likely due to monovalency and lack of affinity maturation (26). The development of high-quality anti-SARS-CoV-2 Nbs may provide a novel means for versatile, cost-effective therapeutics and point-of-care diagnosis.

We report the development and characterization of a collection of diverse, soluble, stable, and high-affinity camelid Nbs that target the RBD. We found that the majority of the high-affinity RBD Nbs can efficiently neutralize the virus. A fraction presents outstanding neutralization potency, comparable with, or better than the most potent human NAbs. We employed an integrative structural approach to map multiple epitopes of neutralizing Nbs. We further determined the crystal structure of an elite Nb of sub-ng/ml neutralization potency in complex with the RBD. Our results revealed that while highly potent neutralizing Nbs predominantly recognize the concave, hACE2 binding site, efficient neutralization can also be accomplished through other

RBD epitopes. Finally, structural characterizations facilitated the bioengineering of multivalent Nbs into multi-epitope cocktails that achieved remarkable neutralization potencies of as low as 0.058 ng/ml (1.3 pM) and may block the mutational escape of the virus.

## Results

### *Development of highly potent SARS-CoV-2 neutralizing Nbs*

To produce high-quality SARS-CoV-2 neutralizing Nbs, we immunized a llama “Wally” with the recombinant RBD protein from human 293T cells. Compared to the pre-bleed, after affinity maturation, the post-immunized serum showed potent and specific serologic activities towards RBD binding with a titer of  $1.75 \times 10^6$  (**Fig S1a**). The serum could efficiently neutralize the pseudotyped SARS-CoV-2 at the half-maximal neutralization titer (NT50) of 310,000 (**Fig S1b**), orders of magnitude higher than the SARS-CoV-2 convalescence individuals’ sera as previously reported (7, 8). To further characterize these activities, we separated the single-chain V<sub>H</sub>H antibodies from the IgG antibodies from the serum. We confirmed that the single-chain antibodies achieve specific, high-affinity binding to the RBD and possess sub-nM half-maximal inhibitory concentration (IC<sub>50</sub> = 509 pM) against the pseudotype virus (**Fig S1c**).

We identified thousands of high-affinity V<sub>H</sub>H Nbs from the RBD-immunized llama serum using a robust proteomic strategy that we have recently developed (27). This repertoire includes ~350 unique CDR3s (complementarity-determining regions). For *E.coli* expression, we selected 109 highly diverse Nb sequences from the repertoire with unique CDR3s to cover various biophysical, structural, and potentially different antiviral properties of our Nb repertoire (**Fig S2a**). 94 Nbs were purified and tested for RBD binding by ELISA, from which we confirmed 71 RBD-specific binders (**Fig S2b-c, Table S1**). Of these RBD-specific binders, 49 Nbs presented high solubility and high-affinity (ELISA IC<sub>50</sub> below 30 nM, **Fig 1a**), and were promising candidates for functional characterizations. We used a SARS-CoV-2-GFP pseudovirus neutralization assay to screen and characterize the antiviral activities of these high-affinity Nbs. Interestingly, the vast majority (94%) of the tested Nbs can neutralize the pseudotype virus below three μM (**Fig 1b**). 90% of them can block the pseudovirus below 500 nM. Only 20-40% of high-affinity RBD-specific mAbs identified from the patients’ sera have been reported to possess comparable potency (7, 8). 76% of the Nbs efficiently neutralized the pseudovirus below 50 nM, and 6% had outstanding neutralization activities below 0.5 nM. We selected the most potent 18 Nbs based on the pseudovirus GFP reporter screen and measured their neutralization potency using the pseudovirus luciferase reporter assay, followed by an authentic SARS-CoV-2 assay for the top 14 neutralizers. As expected, all the Nbs reached 100% neutralization and inhibited the virus’s replication in a dose-dependent manner. The IC<sub>50</sub>s span from single-digit ng/ml to sub- ng/ml, with three unusual neutralizers of Nbs 89, 20, and 21 to be 2.0 ng/ml (0.129 nM), 1.6 ng/ml (0.102 nM), and 0.7 ng/ml (0.045 nM), respectively, based on the pseudovirus assay (**Fig 1c, 1e**). Similar values (0.154 nM, 0.048 nM, and 0.021 nM, for Nbs 89, 20, and 21)

were reproducibly obtained from the authentic virus assay (**Fig 1d, 1e**). There was a strong correlation between the two neutralization assays ( $R^2= 0.92$ , **Fig S3**).

We measured the binding kinetics of Nbs 89, 20, and 21 by surface plasmon resonance (SPR) (**Fig S4a-b**). While Nbs 89 and 20 have an affinity of 108 pM and 10.4 pM, our best-neutralizing Nb21 did not show detectable dissociation from the RBD during 20 min SPR analysis. The femtomolar affinity of Nb21 potentially explains its unusual neutralization potency (**Fig 1f**). We confirmed the excellent thermostability of the top three neutralizing Nbs (89, 20, and 21) from the *E.coli* periplasmic preparations to be 65.9, 71.8, and 72.8°C, respectively (**Fig 43c**). Finally, we tested the on-shelf stability of Nb21, which remained soluble after ~ 6 weeks of storage at room temperature after purification and could well tolerate lyophilization. No multimeric forms or aggregations were detected by size-exclusion chromatography (SEC) (**Fig S4d**). Together these results suggest that our neutralizing Nbs possess outstanding physicochemical properties required for advanced therapeutic applications.

#### *Integrative structural characterization of the Nb neutralization epitopes*

Epitope mapping based on atomic resolution structure determination by X-ray crystallography and Cryo-Electron Microscopy (CryoEM) is highly accurate but low-throughput. Here, we integrated information from SEC, cross-linking mass spectrometry (CXMS), shape and physicochemical complementarity, and statistics to determine structural models of RBD-Nb complexes (28-31). First, we performed SEC experiments to distinguish between Nbs that share the same epitope as Nb21 (thus compete with Nb 21 on an SEC) and those that bind to non-overlapping epitopes (**Fig S5b-j**). Nbs 9, 16, 17, 20, 89, 107, 82, 64, and 99 competed with Nb21 for RBD binding based on SEC profiles (**Fig 2a**), indicating that their epitopes significantly overlap. In contrast, higher mass species (from early elution volumes) corresponding to the trimeric complexes composed of Nb21, RBD, and one of the Nbs (34, 36, 93, 105, and 95) were evident (**Fig 2b**). Moreover, Nb105 competed with Nb34 and Nb95, which did not compete for RBD interaction, suggesting the presence of two distinct and non-overlapping epitopes. Second, we cross-linked Nb-RBD complexes by DSS (disuccinimidyl suberate) and identified on average, four intermolecular cross-links by MS for Nbs 20, 93, 34, 95, and 105. The cross-links were used to map the RBD epitopes derived from the SEC data (**Methods**). Our cross-linking models identified five epitopes (I, II, III, IV, and V corresponding to Nbs 20, 93, 34, 95, and 105) (**Fig 2c**). The models satisfied 90% of the cross-links with an average precision of 7.8 Å (**Fig 2d, Table S2**). Our analysis confirmed the presence of a dominant Epitope I (e.g., epitopes of Nbs 20 and 21) overlapping with the hACE2 binding site. Epitope II also co-localized with the hACE2 binding site, while epitopes III-V did not (**Fig 2e**). Interestingly, epitope I Nbs had significantly shorter CDR3 (four amino acids shorter,  $p = 0.005$ ) than other epitope binders (**Fig S5a**). Despite this, the vast majority of the selected Nbs can potentially inhibit the virus with an IC50 below 30 ng/ml (2 nM) (**Table S1**).

#### *Crystal structure of RBD-Nb20 and analysis of Nbs 20 and 21 interactions with RBD*

To explore the molecular mechanisms that underlie the unusually potent neutralization activities of Epitope I Nbs, we determined a crystal structure of the RBD-Nb20 complex at a resolution of 3.3 Å by molecular replacement (**Methods, Table S3**). Most of the residues in RBD (N334-G526) and the entire Nb20, particularly those at the protein interaction interface, are well resolved. There are two copies of RBD-Nb20 complexes in one asymmetric unit, which are almost identical with an RMSD of 0.277 Å over 287 C $\alpha$  atoms. In the structure, all three CDRs of Nb20 interact with the RBD by binding to its large extended external loop with two short  $\beta$ -strands (**Fig 3a**) (32). E484 of RBD forms hydrogen bonding and ionic interactions with the side chains of R31 (CDR1) and Y104 (CDR3) of Nb20, while Q493 of RBD forms hydrogen bonds with the main chain carbonyl of A29 (CDR1) and the side chain of R97 (CDR3) of Nb20. These interactions constitute a major polar interaction network at the RBD and Nb20 interface. R31 of Nb20 also engages in a cation- $\pi$  interaction with the side chain of F490 of the RBD (**Fig 3b**). In addition, M55 from the CDR2 of Nb20 packs against residues L452, F490, and L492 of RBD to form hydrophobic interactions at the interface). Another small patch of hydrophobic interactions is formed among residues V483 of RBD and F45 and L59 from the framework  $\beta$ -sheet of Nb20 (**Fig 3c**).

The binding mode of Nb20 to the RBD is distinct from other previously reported SARS-CoV-2 neutralizing Nbs, which generally recognize similar epitopes in the RBD external loop region (33, 34, 35) (**Fig S6**). The extensive hydrophobic and polar interactions (**Fig 3b-c**) between the RBD and Nb20 stem from the remarkable shape complementarity (**Fig 3d**) between all the CDRs and the external RBD loop, leading to ultrahigh-affinity ( $\sim 10$  pM). We further modeled the structure of the best neutralizer Nb21 with RBD based on our crystal structure (**Methods**). There are only four residue changes between Nb20 and Nb21 (**Fig S7a**), all of which are on CDRs. Two substitutions are at the RBD binding interface. S52 and M55 in the CDR2 of Nb20 are replaced by two asparagine residues N52 and N55 in Nb21. In our modeled structure, N52 forms a new H-bond with N450 of RBD (**Fig S7b**). While N55 does not engage in additional interactions with RBD, it creates a salt bridge with the side chain of R31, which stabilizes the polar interaction network among R31 and Y104 of Nb21 and Q484 of RBD (**Fig S7b**). All of those may contribute to a slower off-rate of Nb21 vs. Nb20 (**Fig 2f, S4a**) and stronger neutralization potency. Structural comparison of RBD-Nb20/21 and RBD-hACE2 (PDB 6LZG) (32) clearly showed that the interfaces for Nb20/21 and hACE2 partially overlap (**Fig 3d-e**). Notably, the CDR1 and CDR3 of Nb20/21 would severely clash with the first helix of hACE2, the primary binding site for RBD (**Fig 3f**). Our high-resolution structural study provides novel insight into the exceptional binding affinities of epitope I Nbs that are likely to contribute to the sub-ng/ml neutralization potency.

#### *Potential mechanisms of SARS-CoV-2 neutralization by Nbs*

To better understand the outstanding antiviral efficacy of our Nbs, we superimposed RBD-Nb complexes to different spike conformations based on cryoEM structures. We found that three copies of Nb20/21 can simultaneously bind all three RBDs in their “down” conformations (PDB 6VXX) (4) that correspond to the spike’s inactive state (**Fig 4b**). Our analysis indicates a potential mechanism by which Nbs

20 and 21 (Epitope I) lock RBDs in their down conformation with ultrahigh affinity. Combined with the steric interference with hACE2 binding in the RBD open conformation (**Fig 4a**), these mechanisms may explain the extraordinary neutralization potencies of Epitope I Nbs.

Other epitope-binders do not fit into this inactive conformation without steric clashes and appear to utilize different neutralization strategies (**Fig 4c**). For example, Epitope II: Nb 93 co-localizes with hACE2 binding site and can bind the spike in the one RBD “up” conformation (**Fig 4d**, PDB 6VSB) (3). It may neutralize the virus by blocking the hACE2 binding site. Epitope III and IV Nbs can only bind when two or three RBDs are at their “up” conformations (PDB 6XCN) (26) where the epitopes are exposed. In the all RBDs “up” conformation, three copies of Nbs can directly interact with the trimeric spike. Interestingly, through RBD binding, Epitope III: Nb34 can be accommodated on top of the trimer to lock the helices of S2 in the prefusion stage, preventing their large conformational changes for membrane fusion (**Fig 4e**). When superimposed onto the all “up” conformation, Epitope IV: Nb95 is proximal to the rigid NTD of the trimer, presumably restricting the flexibility of the spike domains (**Fig 4f**).

#### *Development of flexible, multivalent Nbs for highly efficient viral neutralization*

Epitope mapping enabled us to bioengineer a series of multivalent Nbs (**Fig 5a**). Specifically, we designed two sets of constructs that build upon our most potent Nbs. The homotrimeric Nbs, in which a flexible linker sequence (either 31 or 25 amino acids, **Methods**) separates each monomer Nb (such as Nb21 or Nb20), were designed to increase the antiviral activities through avidity binding to the virion trimeric spikes. The heterodimeric forms that conjugate two Nbs of unique, non-overlapping epitopes, through a flexible linker of 12 residues.

We synthesized a variety of constructs and tested their neutralization potency. We found up to ~30 fold improvement for the homotrimeric constructs of Nb21<sub>3</sub> (IC<sub>50</sub> =1.3 pM) and Nb20<sub>3</sub> (IC<sub>50</sub> =3 pM) compared to the respective monomeric form by the pseudovirus luciferase assay (**Fig 5b, 5d**). Similar results were obtained from the authentic virus assay (**Fig 5c, 5d**). The improvements are likely greater than these values indicate, as the measured values may reflect the assay’s lower detection limits. For the heterodimeric constructs, up to a 4-fold increase of potency (i.e., Nb21-Nb34) was observed. Importantly, the multivalent constructs retained outstanding physicochemical properties of the monomeric Nbs, including high solubility, yield, and thermostability (**Fig S8**). They remained fully active after standard lyophilization and nebulization (**Methods, Fig S9**), indicating the outstanding stability and flexibility of administration. The majority of the RBD mutations observed in GISAID (36) are very low in frequency (<0.0025). Therefore, the probability of mutational escape with a cocktail consisting of 2-3 Nbs covering different epitopes is extremely low (**Fig 5e**) (9).

## **Discussion**

The development of effective, safe, and inexpensive vaccines and therapeutics may provide solutions to end the COVID-19 crisis. Here, *in vivo* (camelid) antibody affinity maturation followed by advanced proteomics (27) enabled rapid identification of a large repertoire of diverse, high-affinity RBD Nbs for the neutralization of SARS-CoV-2. We found that most of the high-affinity Nbs efficiently neutralize the virus; some elite Nbs in their monomeric forms can inhibit the viral infection at single-digit to sub-ng/ml concentrations.

We identified multiple neutralization epitopes through the integration of biophysics, structural proteomics, modeling, and X-ray crystallography. We have gained novel insight into the mechanisms by which Nbs target the RBD with femtomolar affinity to achieve remarkable neutralization potency. Our structural analysis revealed that the hACE2 binding site correlates with immunogenicity and neutralization. While the most potent Nbs inhibit the virus by high-affinity binding to the hACE2 binding site, we also observed other neutralization mechanisms through non-hACE2 epitopes.

During our manuscript preparation, a preprint reported an extensively bioengineered, homotrimeric Nb construct reaching antiviral activity comparable to our single monomeric Nb20 (21). Here, we have developed a collection of novel multivalent Nb constructs with outstanding stability and neutralization potency at double-digit pg/ml. To our knowledge, this represents the most potent biotherapeutics for SARS-CoV-2 available to date. The use of multivalent, multi-epitope Nb cocktails may prevent virus mutational escape (37-39). Flexible and efficient administration, such as direct inhalation, may further improve antiviral drug efficacy while minimizing the dose, cost, and potential toxicity for clinical applications. The high sequence similarity between Nbs and IgGs may restrain the immunogenicity (40). For intravenous drug delivery, it is possible to fuse our antiviral Nbs with the albumin-Nb constructs (41) that we have developed to improve the *in vivo* half-lives. Our Nbs can also be applied as rapid point-of-care diagnostics due to the high stability, specificity, and low cost of manufacturing. We envision that these high-quality Nb agents will contribute to curbing the current pandemic.

## Figures and Figure Legends

## Figure 1

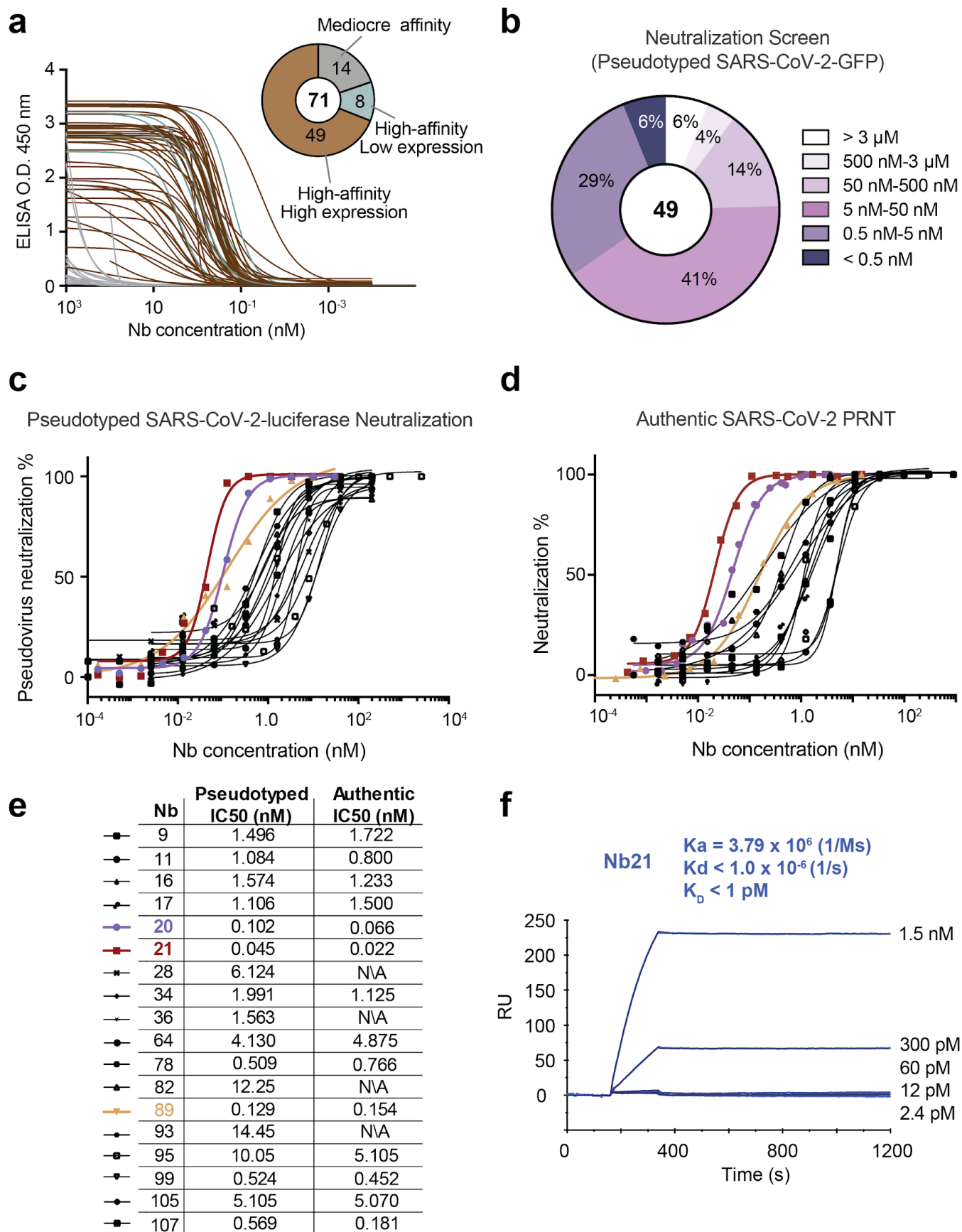




## **Figure 1. Production and characterizations of high-affinity RBD Nbs for SARS-CoV-2 neutralization**

**1a:** The binding affinities of 71 Nbs towards RBD by ELISA. The pie chart shows the number of Nbs according to affinity and solubility.

**1b:** Screening of 49 soluble, high-affinity Nbs by SARS-CoV-2-GFP pseudovirus neutralization assay. n = 1 for Nbs with neutralization potency  $IC_{50} \leq 50$  nM, n = 2 for Nbs with neutralization potency  $IC_{50} > 50$  nM.

**1c:** The neutralization potency of 18 highly potent Nbs was calculated based on the pseudotyped SARS-CoV-2 neutralization assay with Luciferase reporter. Purple, red, and orange lines denote Nbs 20, 21, and 89 with  $IC_{50} < 0.2$  nM. Two different purifications of the pseudovirus were used. The average neutralization % was shown for each data point (n = 5 for Nbs 20, 21; n=2 for all other Nbs).

**1d:** The neutralization potency of the top 14 neutralizing Nbs by authentic SARS-CoV-2 plaque reduction neutralization test (PRNT). The average neutralization % was shown for each data point (n=4 for Nbs 20, 21, and 89; n=2 for other Nbs).

**1e:** A table summary of pseudotyped and authentic SARS-CoV-2 neutralization potency for 18 Nbs. N/A: not tested.

**1f:** The SPR binding kinetics measurement of Nb21.

## Figure 2

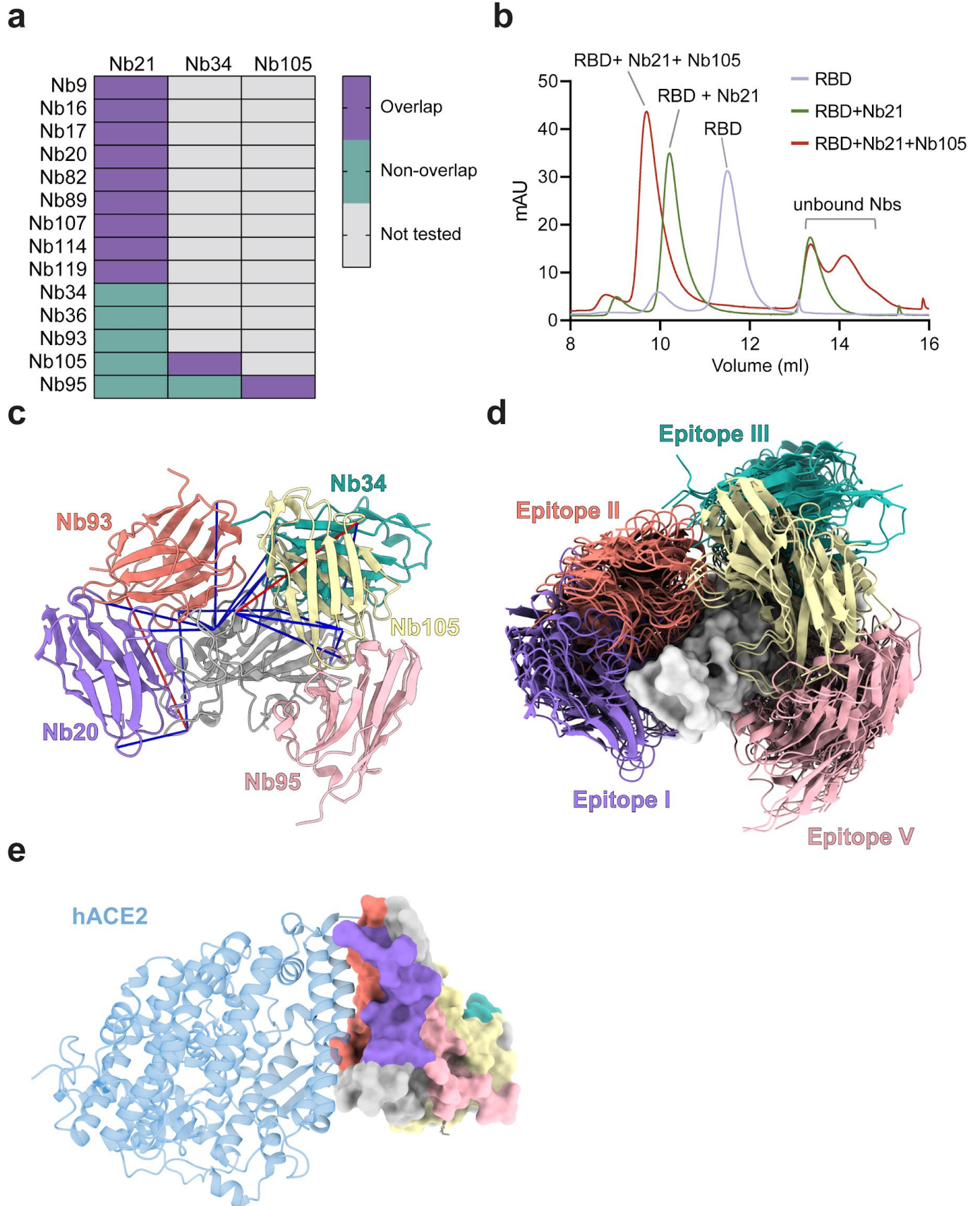


## Figure 2. Nb epitope mapping by integrative structural proteomics

**Fig 2a:** A summary of Nb epitopes based on size exclusion chromatography (SEC) analysis. Light salmon color: Nbs that bind the same RBD epitope. Sea green: Nbs of different epitopes.

**Fig 2b:** A representation of SEC profiling of RBD, RBD-Nb21 complex, and RBD-Nb21-Nb105 complex. The y-axis represents UV 280 nm absorbance units (mAu).

**Fig 2c:** A cartoon model showing the localization of five Nbs that bind different epitopes: Nb20 (medium purple), Nb34 (light sea green), Nb93 (salmon), Nb105 (pale goldenrod) and Nb95 (light pink) in complex with the RBD (gray). Blue and red lines represent DSS cross-links shorter or longer than 28Å, respectively.

**Fig 2d:** Top 10 scoring cross-linking based models for each Nb (cartoons) on top of the RBD surface.

**Fig 2e:** The surface display of different Nb neutralization epitopes on the RBD in complex with hACE2 (cartoon model in blue).

Figure 3

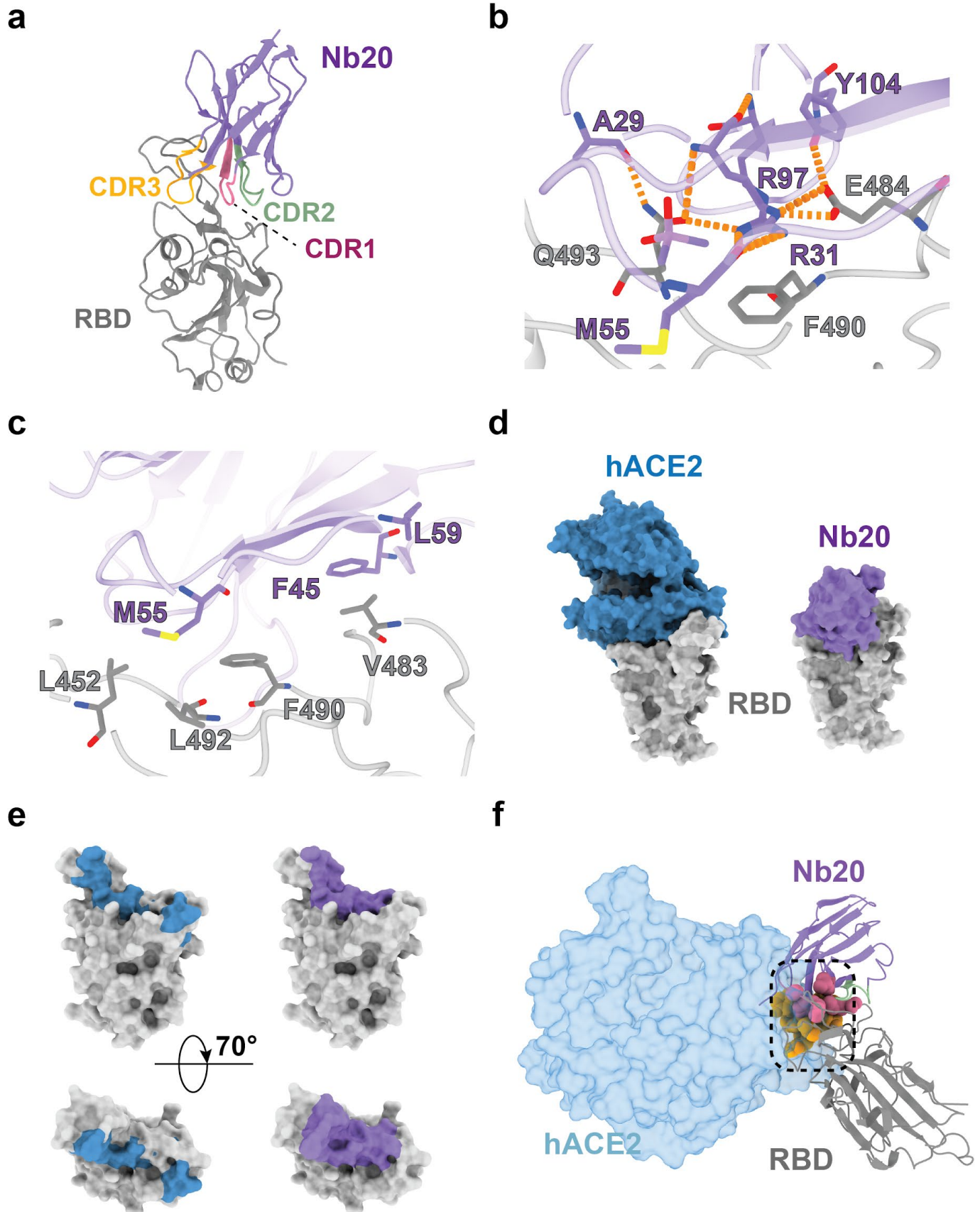


### **Figure 3. Crystal structure analysis of an ultrahigh affinity Nb in complex with the RBD**

**3a.** Cartoon presentation of Nb20 in complex with the RBD. CDR1, 2, and 3 are in red, green, and orange, respectively.

**3b.** Zoomed-in view of an extensive polar interaction network that centers around R35 of Nb20.

**3c.** Zoomed-in view of hydrophobic interactions.

**3d.** Surface presentation of the Nb20-RBD and hACE2-RBD complex (PDB: 6M0J)

**3e.** Surface presentation of RBD with hACE2 binding epitope colored in steel blue and Nb20 epitope colored in medium purple.

**3f.** The CDR1 and CDR3 residues (medium violet pink and light goldenrod in spheres, respectively) of Nb20 overlap with hACE2 binding site (light blue) on the RBD (gray).

## Figure 4

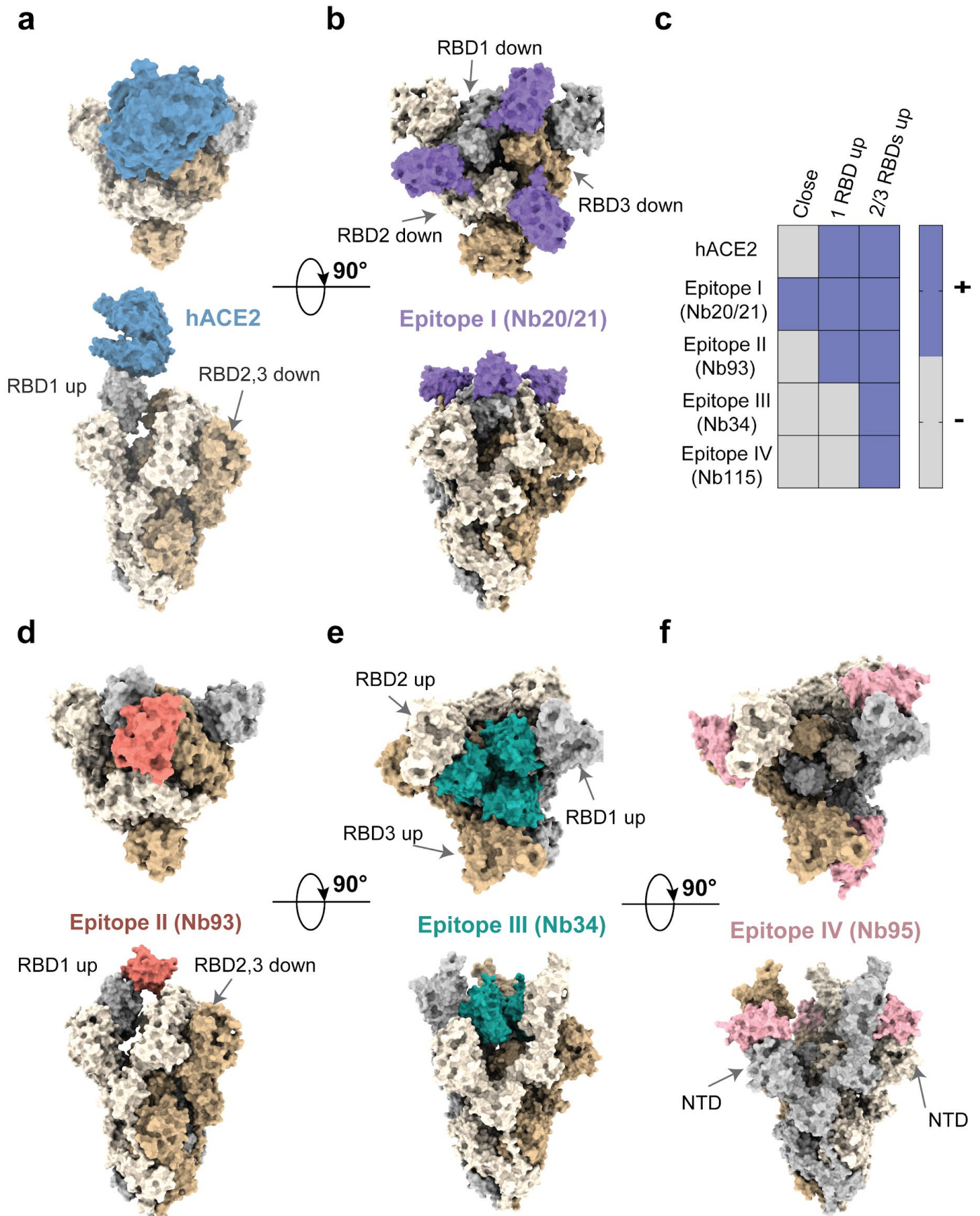


**Figure 4. Potential mechanisms of SARS-Cov-2 neutralization by Nbs.**

**4a.** hACE2 (grey) binding to spike trimer conformation (wheat, plum, and light blue colors) with one RBD up (PDBs 6VSB, 6LZG).

**4b.** Nb20 (Epitope I, medium purple) partially overlaps with the hACE2 binding site and can bind the closed spike conformation with all RBDs down (PDB 6VXX).

**4c.** A summary of spike conformations accessible (+) to the Nbs of different epitopes.

**4d.** Nb93 (Epitope II, salmon) partially overlaps with the hACE2 binding site and can bind to spike conformations with at least one RBD up (PDB 6VSB).

**4e-f.** Nb34 (Epitope III, light sea blue) and Nb95 (Epitope IV, light pink) do not overlap with the hACE2 binding site and bind to spike conformations with at least two open RBDs (PDB 6XCN).

## Figure 5

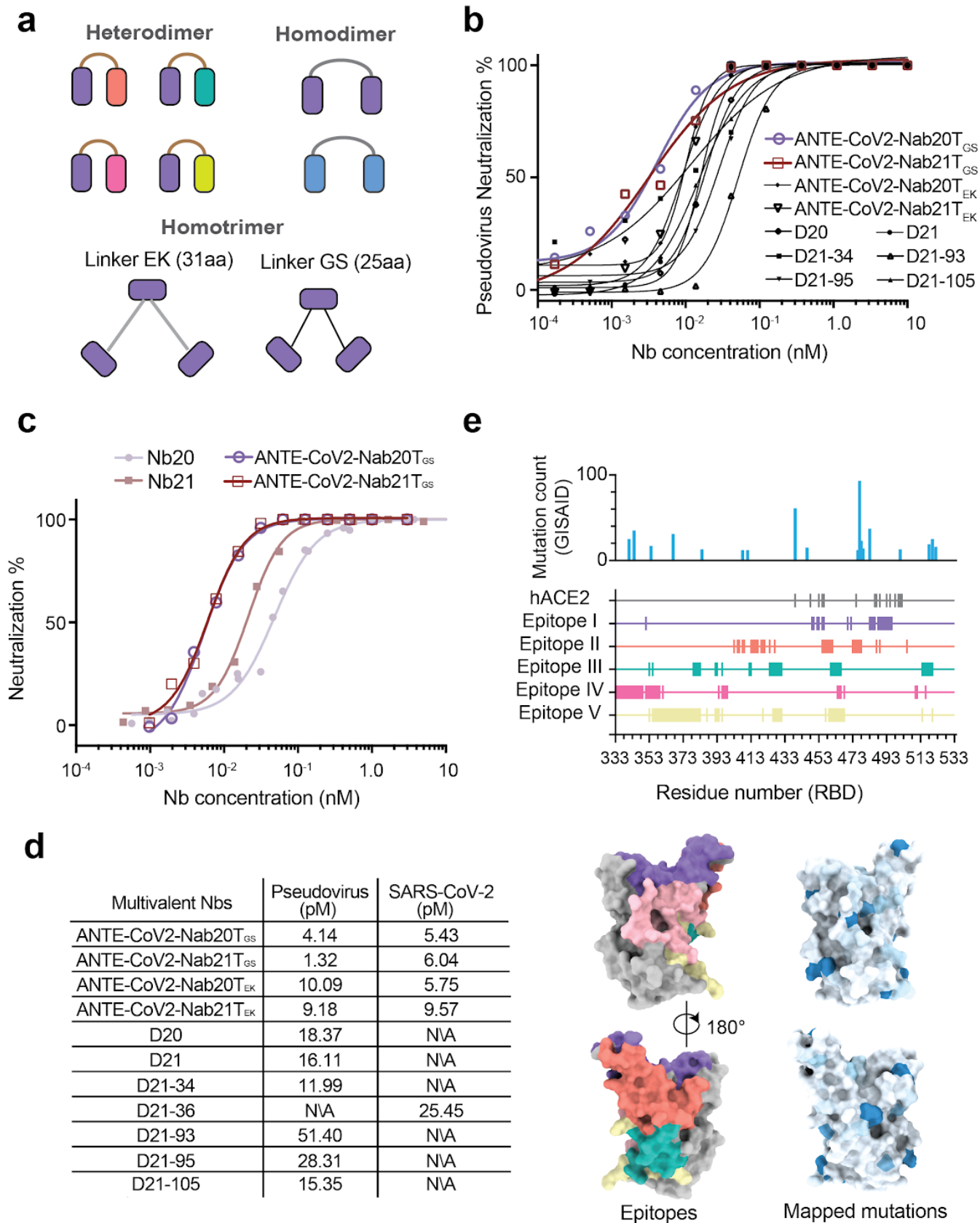




## Figure 5. Development of multivalent Nb cocktails for highly efficient SARS-CoV-2 neutralization

**Fig 5a:** Schematics of the cocktail design

**Fig 5b:** Pseudotyped SARS-CoV-2 neutralization assay of multivalent Nbs. The average neutralization % of each data point was shown (n=2).

**Fig 5c:** Authentic SARS-CoV-2 PRNT of monomeric and trimeric forms of Nbs 20 and 21. The average neutralization % of each data point was shown (n=2 for the trimer constructs, n=4 for the monomers).

**Fig 5d:** A summary table of the neutralization potency measurements of the multivalent Nbs. N/A: not tested.

**Fig 5e:** Mapping mutations to localization of Nb epitopes on the RBD. The x-axis corresponds to the RBD residue numbers (333 to 533). Rows in different colors represent different epitope residues. Epitope I: 351, 449-450, 452-453, 455-456, 470, 472, 483-486, 488-496; Epitope II: 403, 405-406, 408,409, 413-417, 419-421, 424, 427, 455-461, 473-478, 487, 489, 505; Epitope III: 53, 355, 379-383, 392-393, 396, 412-413, 424-431, 460-466, 514-520; Epitope IV: 333-349, 351-359, 361, 394, 396-399, 464-466, 468, 510-511, 516; Epitope V: 353, 355-383, 387, 392-394, 396, 420, 426-431, 457,459-468, 514, 520

## Acknowledgments

We thank the staff at the GM/CA of APS in the Argonne National Laboratory (US) for their assistance with X-ray diffraction data collection. We thank Prof. Zhiyi Wei at the Southern University of Science and Technology for help with crystal structure determination. This work was supported by the University of Pittsburgh School of Medicine (Y.S.), CTSI pilot fund (Y.S.), NIH grant R35GM128641 (C.Z.), ISF 1466/18 (D.S.), and Israeli Ministry of Science and Technology (D.S.).

## Contributions

Y.S. and D.S. conceived the study. Y.X. performed most of the experiments. S.N. performed the authentic virus assay with the help of Y.X. Z.X. produced the multivalent Nbs and performed thermostability measurements. C.Z. determined the X-ray structure. Y.X., Y.S., D.S., C.Z., Z.S., S.N., and P.D. analyzed the data. Y.S. cheerled the study and drafted the manuscript. All authors edited the manuscript.

## Competing interests

The University of Pittsburgh has filed a provisional patent in connection with the manuscript.

## Supplemental Materials

### Versatile, Multivalent Nanobody Cocktails for Highly Efficient SARS-CoV-2 Neutralization

Yufei Xiang<sup>1</sup>, Shamkumar Nambulli #<sup>2</sup>, Zhengyun Xiao #<sup>1</sup>, Heng Liu #<sup>4</sup>, Zhe Sang<sup>1,3</sup>, Paul Duprex<sup>2</sup>, Dina Schneidman-Duhovny<sup>5</sup>, Cheng Zhang<sup>4</sup>, and Yi Shi<sup>1,3</sup>

6. Department of Cell Biology
7. Center for Vaccine Research
8. Pitt/CMU Program for Computational Biology
9. Department of Pharmacology and Chemical Biology  
University of Pittsburgh, Pittsburgh, PA, USA
10. School of Computer Science and Engineering, Institute of Life Sciences, The Hebrew University of Jerusalem, Israel

## Supplemental Figure 1

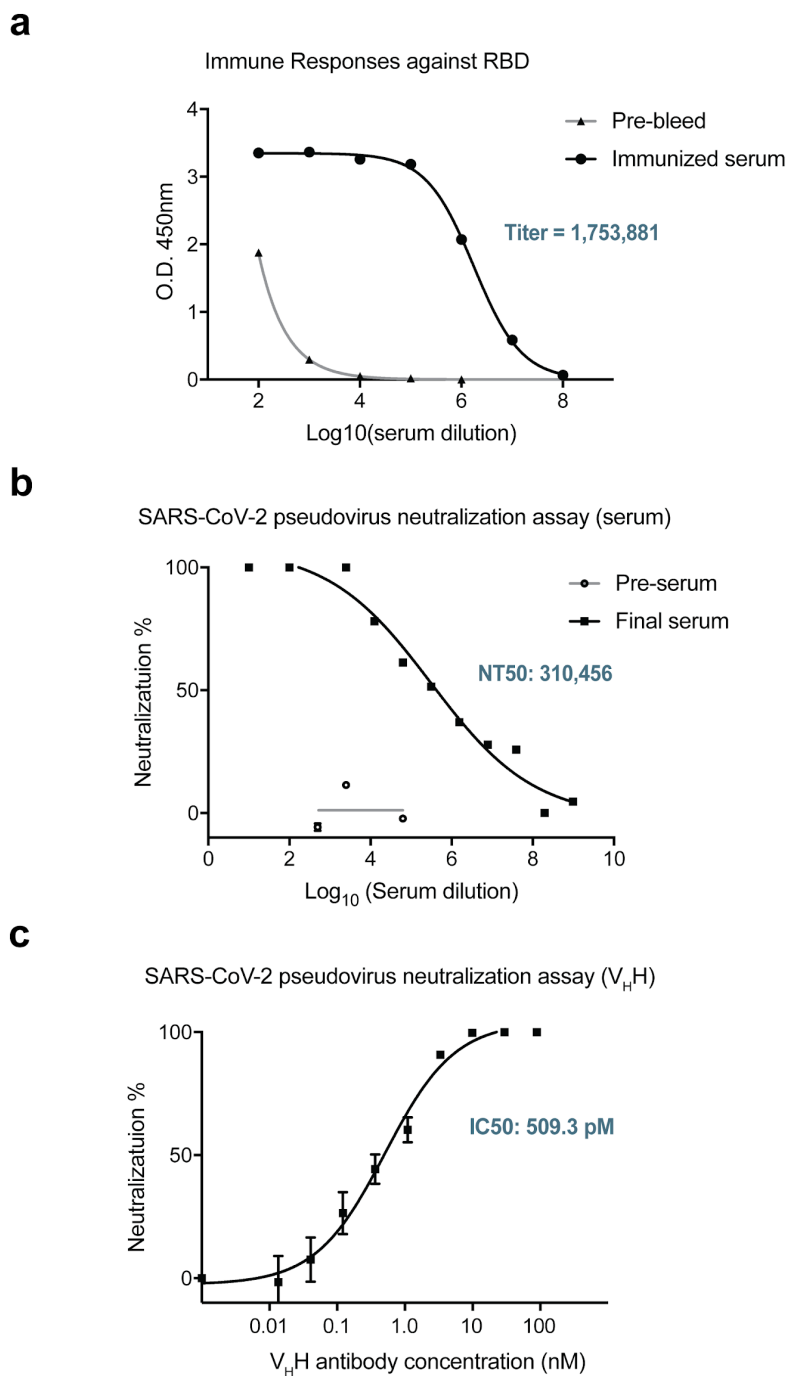


### Figure S1. Development of RBD-specific Nbs for potent SARS-CoV-2 neutralization

S1a: Detection of strong and specific serologic activities after immunization of SARS-CoV-2<sub>RBD</sub>

S1b: Neutralization potency of the immunized camelid's serum against pseudotyped SARS-CoV-2 (Luciferase)

S1c: Neutralization potency of Nbs against pseudotyped SARS-CoV-2 (Luciferase)

## Supplemental Figure 2

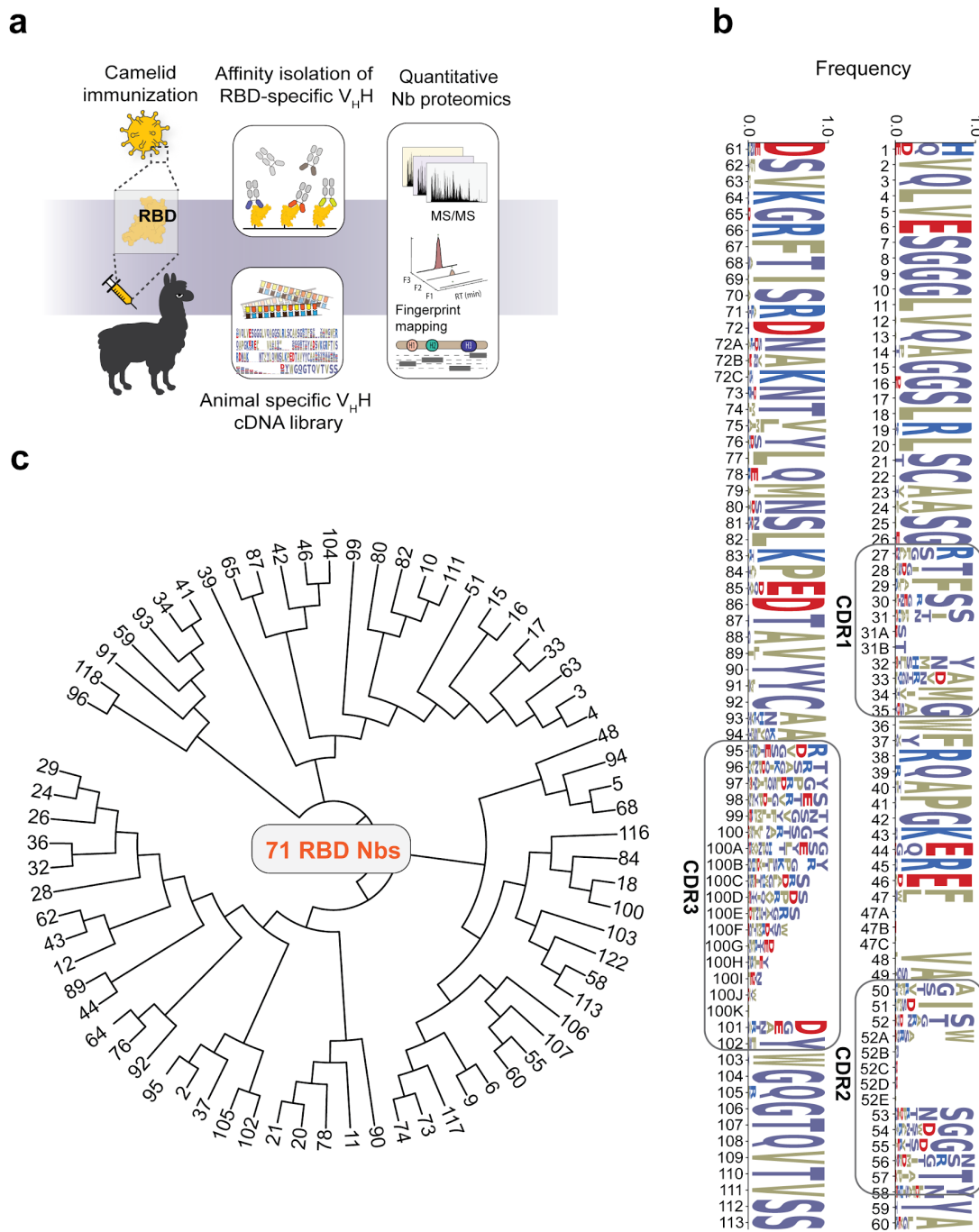


### Figure S2. Identification of a large repertoire of high-affinity Nbs by proteomics

S2a: The schematic of high-affinity RBD-Nb identification by camelid immunization and quantitative Nb proteomics. Briefly, a camelid was immunized by the RBD. High-affinity, RBD-specific single-chain V<sub>H</sub>H antibodies were affinity isolated from the immunized serum, and analyzed by quantitative proteomics to identify the high-affinity, RBD-specific Nbs (see Methods). A V<sub>H</sub>H (Nb) cDNA library from the plasma B cells of the immunized camelid was generated to facilitate proteomic analysis.

S2b: Sequence logo of 71 RBD Nbs. Each Nb has a unique CDR3 sequence. The amino acid occurrence at each position is shown. CDR: complementarity determining region. FR: framework.

S2c: The phylogenetic tree of the Nbs constructed by the maximum likelihood model.

## Supplemental Figure 3

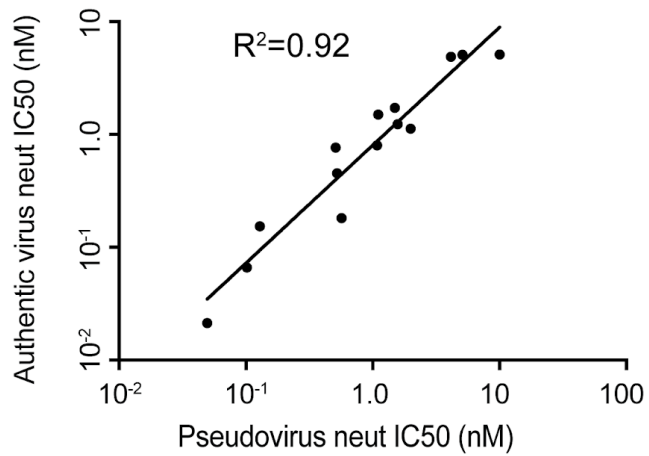


### Figure S3. Correlation analysis of 18 highly potent SARS-CoV-2 neutralizing Nbs.

A plot showing a linear correlation of Nb neutralization IC50s between two pseudotype virus assay and the authentic virus assay.

## Supplemental Figure 4

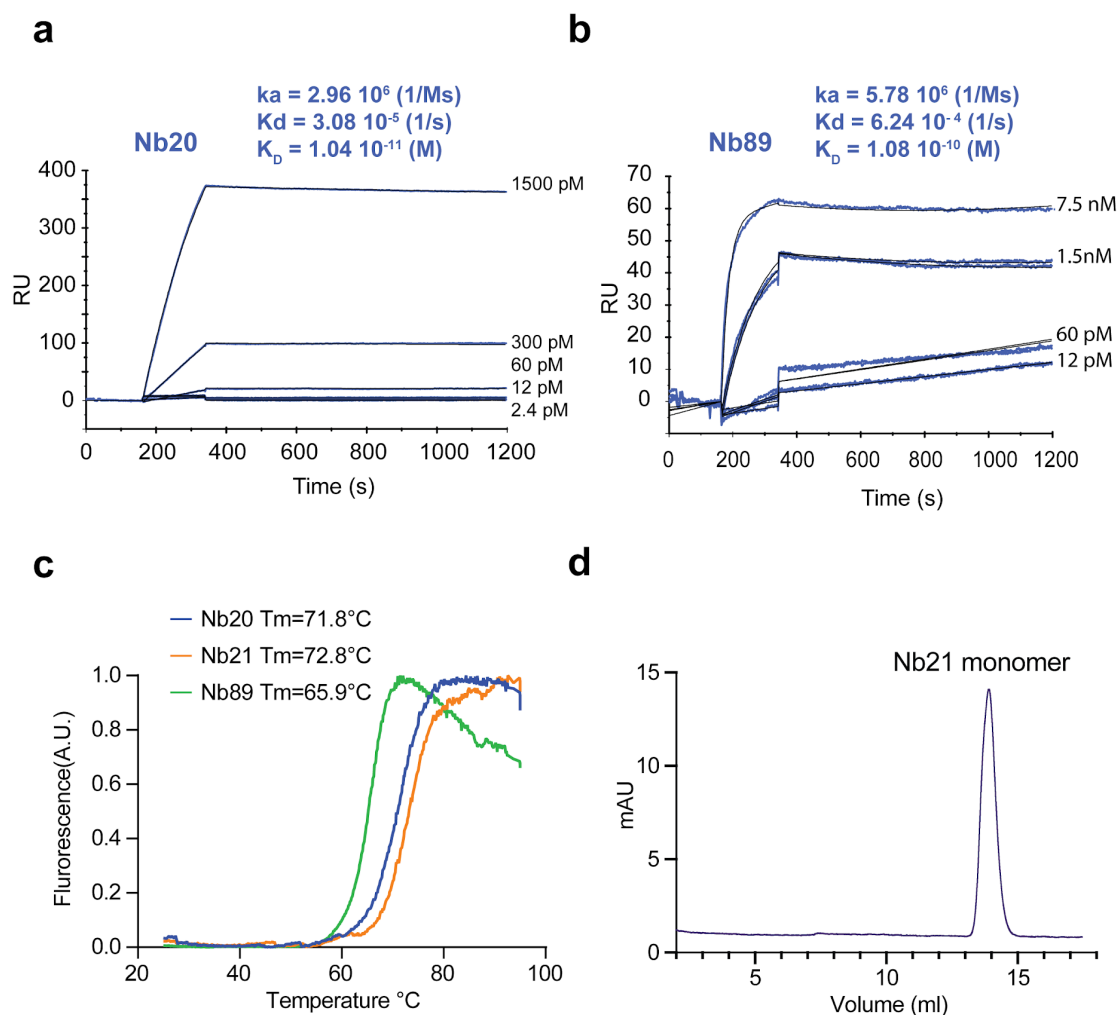


### Figure S4. Biophysical analysis of the outstanding neutralizing Nbs

S4a-b: Binding kinetics of Nbs 20 and 89 by SPR.

S4c: Thermostability analysis of Nbs 20, 21, and 89. The values represent the average thermostability ( $T_m$ , °C) based on three replicates. The standard deviations (SD) of the measurements are 0.17, 0.93, and 0.8 °C for Nbs 20, 21, and 89.

S4d: Stability analysis of Nb21 by SEC. Purified recombinant Nb21 was stored at room temperature for ~ 6 weeks before subject to SEC analysis. The dominant peak represents Nb 21 monomer.

## Supplemental Figure 5

**a**

```

82 NTLNSQLLPR-----AY
99 RTGSG-----VY
107 RSATTALY-----DY
89 RNPGTGQY-----DY
78 RNIETA EY-----TY
11 RNLETFDY-----TY
20 RDIETA EY-----IY
21 RDIETA EY-----TY
9 SHGVVDGTSVNGY----RY
64 GPRLGSTPRAY-----DY
17 VGQEASAYAPR-----AY
16 VAYDYSWGRPR-----NF
105 RRDSSWGYSRDLFEY--DY
34 SKDPYGGSPWTRSEFD--DY
93 CRQEFSSWDFSSRDPDDFDY
28 ETYSLYEKSDSW----GY
36 ETYSIYEKDDSW----GY
95 DKDVIYGYTSFPNEY--EY
    
```

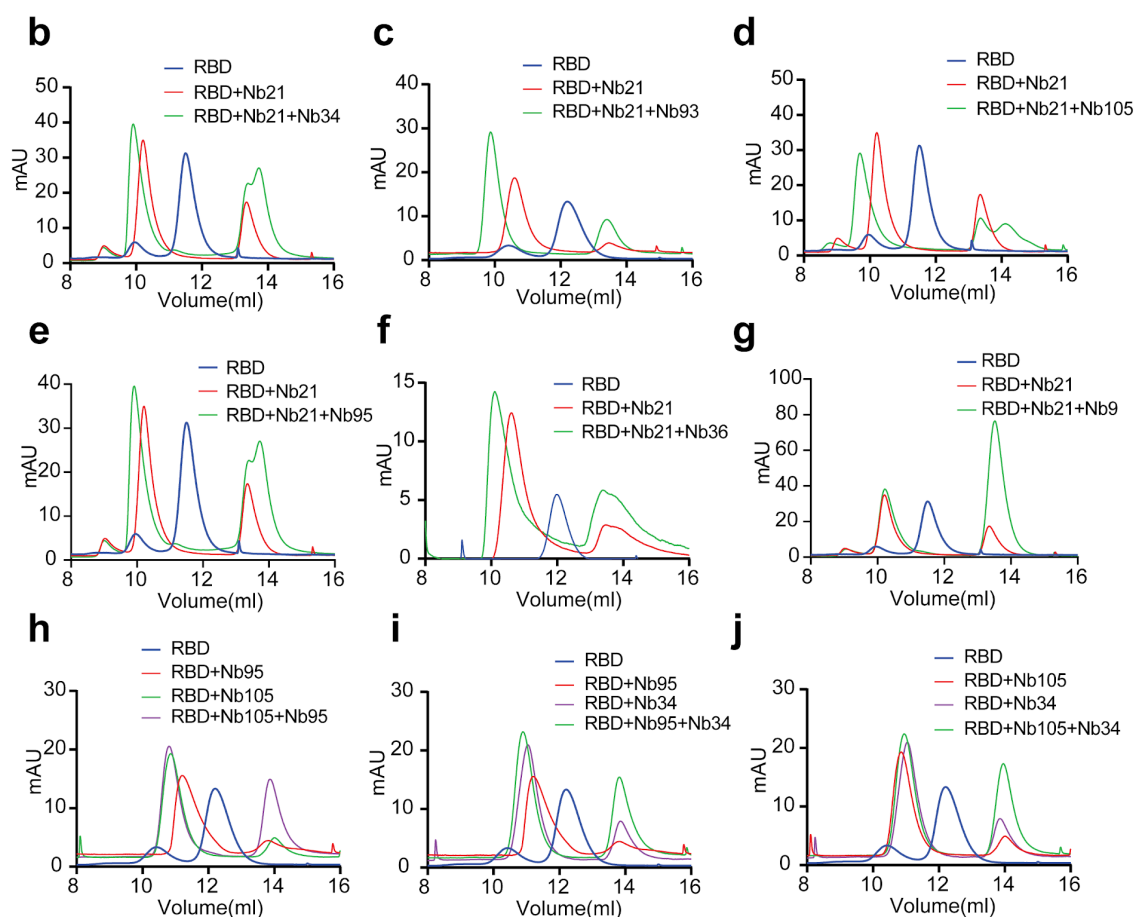
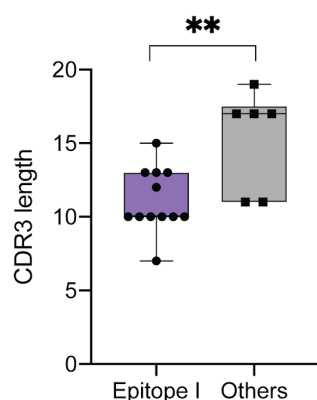


**Figure S5. SEC analysis of RBD-Nb complexes**

S5a: Sequence alignment of the CDR3s of 18 highly potent neutralizing Nbs and CDR3 lengths comparing Nbs from epitope I and others.

S5b-j: The SEC profiles of RBD-Nb complexes to screen for epitopes on RBD.

## Supplemental Figure 6

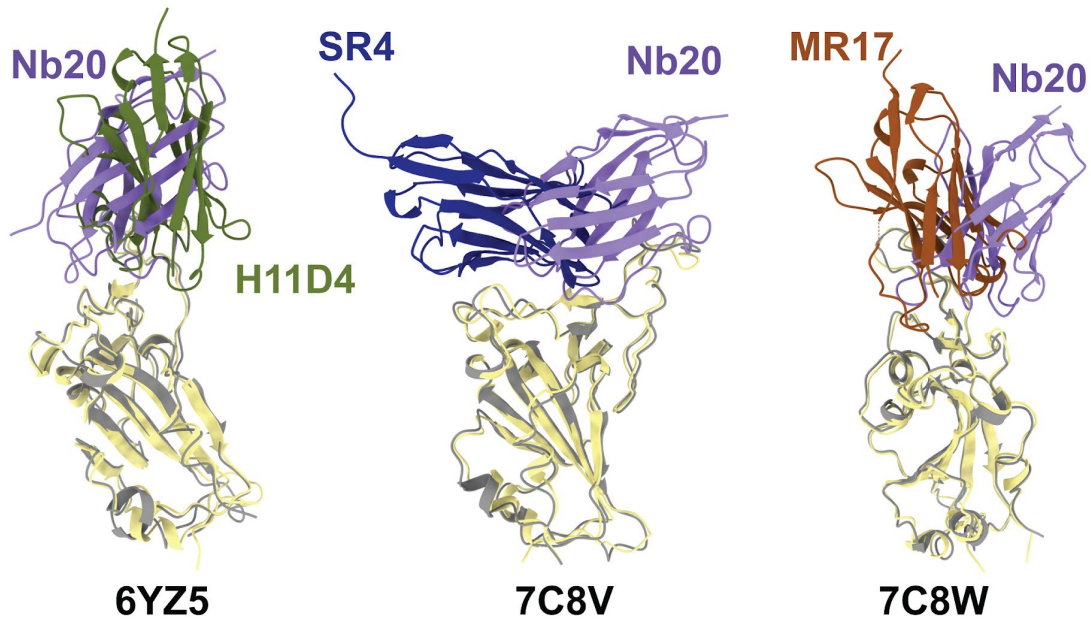


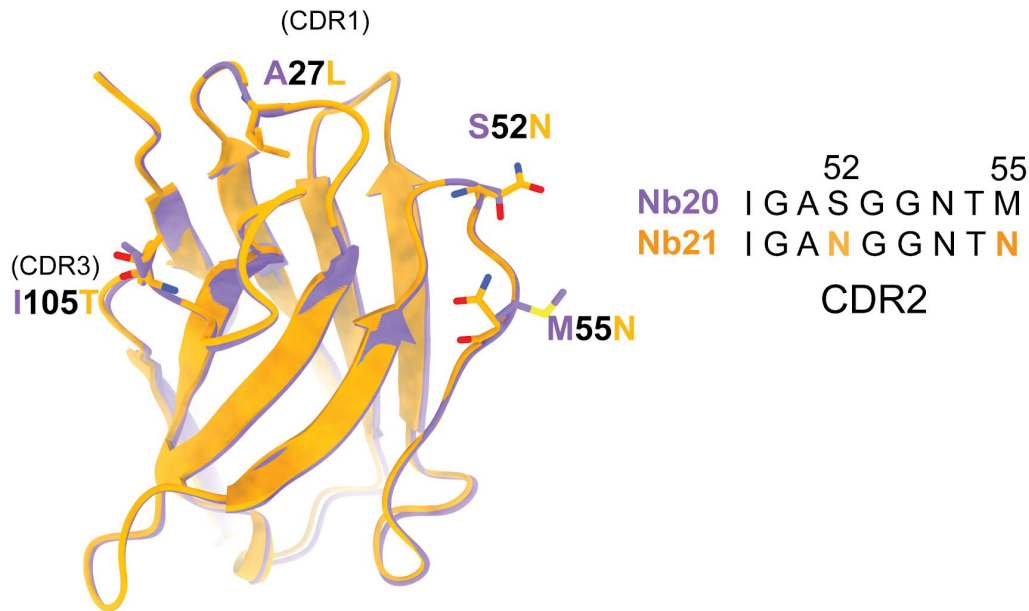
**Figure S6. Structural comparisons of Nb 20 with published RBD Nb structures**

Overlays of Nb 20 (green ribbon) and three other RBD-Nbs (PDBs 6YZ5, 7C8V, and 7C8W) in complex with RBD (yellow ribbon).



## Supplemental Figure 7

a



b

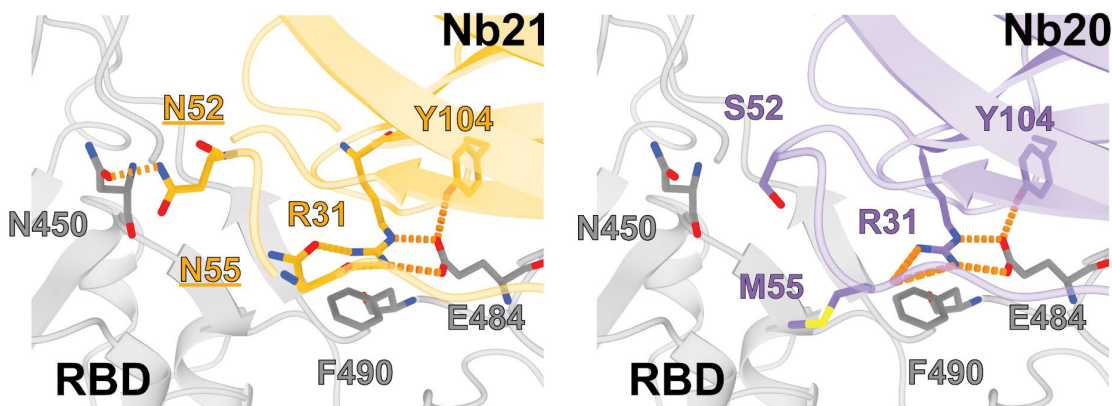


**Figure S7. Modeling of Nb 21-RBD interaction based on the crystal structure of Nb 20-RBD complex**

S7a: Alignment of Nb21 with Nb20. The four residue differences were shown.

S7b: Zoom-in views showing the addition of new polar interaction between N52 (Nb21) and N450 (RBD). The model of Nb21 is superimposed based on the crystal structure of Nb20.

## Supplemental Figure 8

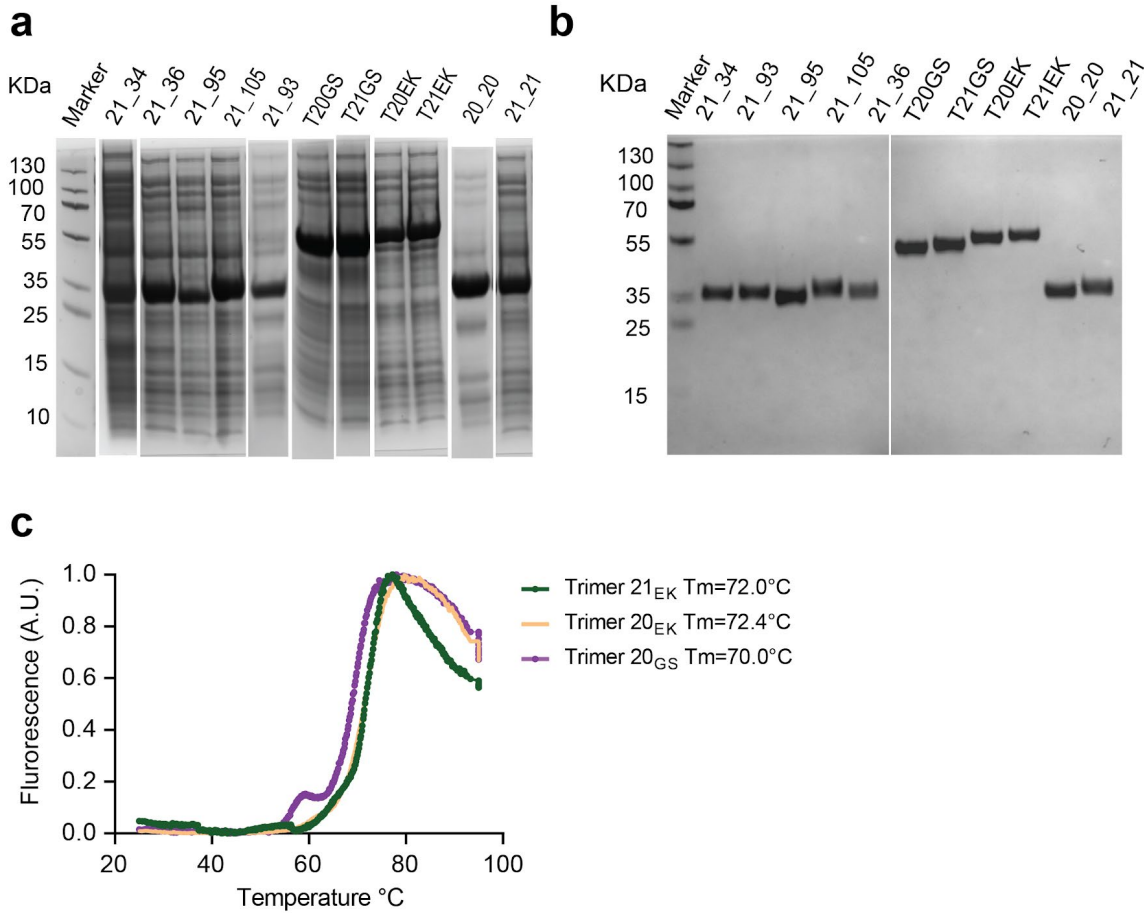


### Figure S8. The biophysical properties of multivalent Nbs

S8a: The expression levels of multivalent Nbs from *E.coli* whole cell lysate.

S8b: A SDS-PAGE gel picture showing the purification of the multivalent Nbs.

S8c: Thermostability analysis of ANTE-CoV2-Nab21<sub>EK</sub>, ANTE-CoV2-Nab20<sub>EK</sub>, and ANTE-CoV2-Nab20<sub>GS</sub>.

The values represent the average thermostability (T<sub>m</sub>, °C) based on three replicates. The standard deviations of the measurement are 0.6, 0.27, and 0.72°C, respectively.

## Supplemental Figure 9

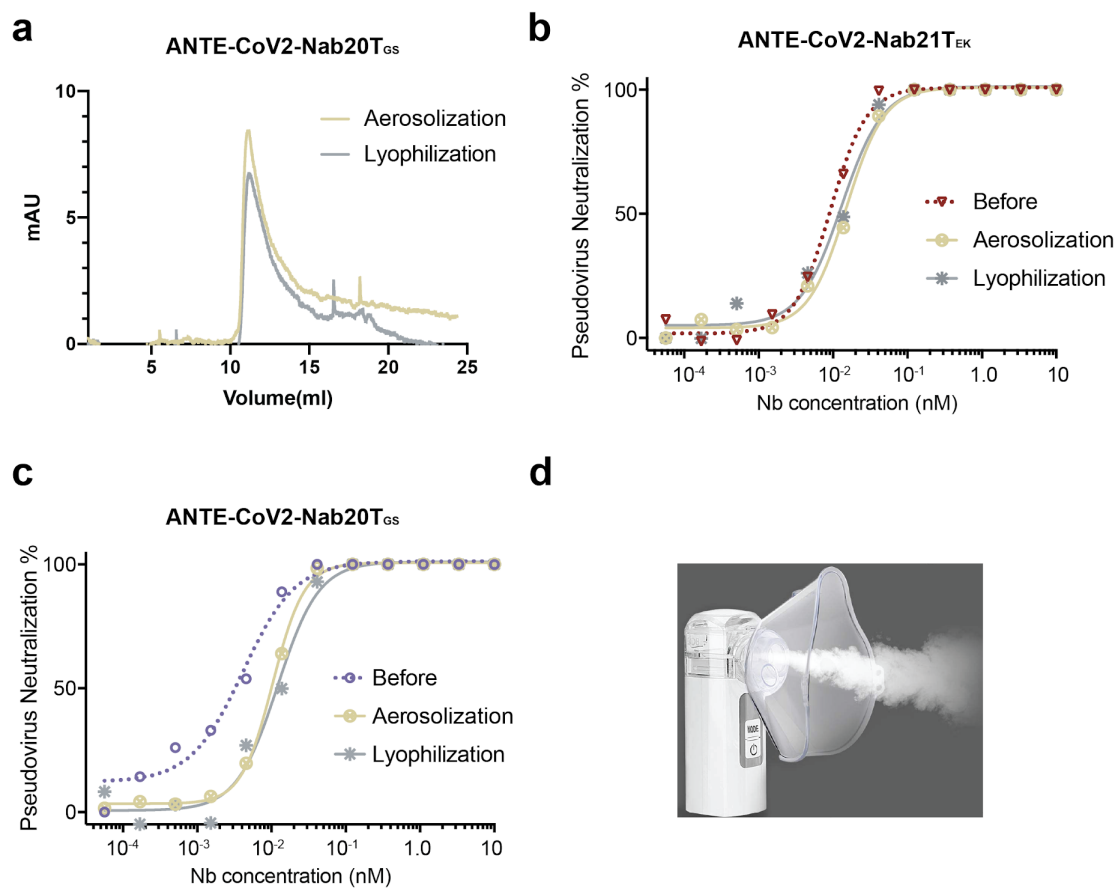


### Figure S9. Stability test of the multivalent Nbs

S9a: The example SEC analyses of ANTE-CoV2-Nab20T<sub>GS</sub> after lyophilization and aerosolization.

S9b: Pseudotyped SARS-CoV-2 neutralization assay using ANTE-CoV2-Nab21T<sub>EK</sub> before and after lyophilization and aerosolization.

S9c: Pseudotyped SARS-CoV-2 neutralization assay using ANTE-CoV2-Nab20T<sub>GS</sub> before and after lyophilization and aerosolization.

S9d: A picture of the portable mesh nebulizer used in the study.

**Supplemental Table 1.** Summary of the synthesized 71 RBD-Nbs.

**Supplemental Table 2.** Summary of the cross-links of the Nbs from different epitopes.

**Supplemental Table 3.** X-ray diffraction data collection and refinement statistics

## Supplemental Table 3

	SARS-CoV-2 RBD with Nb20 (PDB code: 7JVB)
<b>Data collection</b>	
Space group	$P4_12_12$
Cell dimensions	
$a, b, c$ (Å)	70.716, 70.716, 435.037
$\alpha, \beta, \gamma$ (°)	90, 90, 90
Resolution (Å)	40-3.3 (3.36-3.30)
$R_{\text{merge}}$ (%) <sup>a</sup>	15.6 (59.1)
$I/\sigma(I)$	7.8 (1.1)
$CC_{1/2}$ <sup>b</sup>	1(0.811)
Completeness (%)	97.1 (81.4)
Redundancy	6.2 (3.4)
<b>Refinement</b>	
Resolution (Å)	38.96-3.287 (3.405-3.287)
No. reflections	17336 (1377)
$R_{\text{work}} / R_{\text{free}}$ (%) <sup>c</sup>	28.7 (38.2) / 32.2 (43.0)
No. atoms	
Protein	4728
Ligand/ion	20
Water	0
<i>B</i> factors	
Protein	133.33
Ligand/ion	120.40
Water	N/A
R.m.s. deviations	
Bond lengths (Å)	0.005
Bond angles (°)	1.57
Ramachandran analysis	
Favored region (%)	92.16
Allowed region (%)	7.84
Outliers (%)	0

The numbers in parentheses represent values for the highest resolution shell.

<sup>a</sup> $R_{\text{merge}} = \sum |I_i - I_m| / \sum I_i$ , where  $I_i$  is the intensity of the measured reflection and  $I_m$  is the mean intensity of all symmetry-related reflections.

<sup>b</sup> $CC_{1/2}$  is the correlation coefficient of the half datasets.

<sup>c</sup> $R_{\text{work}} = \sum ||F_{\text{obs}}| - |F_{\text{calc}}|| / \sum |F_{\text{obs}}|$ , where  $F_{\text{obs}}$  and  $F_{\text{calc}}$  are observed and calculated structure factors.

$R_{\text{free}} = \sum T ||F_{\text{obs}}| - |F_{\text{calc}}|| / \sum T |F_{\text{obs}}|$ , where T is a test data set of about 5% of the total reflections randomly chosen and set aside prior to refinement.

### Materials and methods

#### *Camelid immunization and proteomic identification of high-affinity RBD-Nbs*

A male Llama “Wally” was immunized with an RBD-Fc fusion protein (Acro Biosystems, Cat#SPD-c5255). The bleeds from the animal were collected after a 55-day immunization protocol (Capralogics, Inc. ). All the above procedures were performed by following the IACUC protocol.  $\sim 1 \times 10^9$  peripheral mononuclear cells were isolated from 350 ml immunized blood using Ficoll gradient (Sigma). The mRNA was purified from the mononuclear cells using an RNeasy kit (Qiagen) and was reverse-transcribed into cDNA by the Maxima™ H

Minus cDNA Synthesis kit (Thermo). The VHH genes were PCR amplified, and the P5 and P7 adapters were added with the index before sequencing. Next-generation sequencing (NGS) of the VHH repertoire was performed by Illumina MiSeq with the 300 bp paired-end model.

For proteomic analysis of RBD-specific Nbs, plasma was first purified from the immunized blood by the Ficoll gradient (Sigma). V<sub>H</sub>H antibodies were then isolated from the plasma by a two-step purification protocol using protein G and protein A sepharose beads (Marvelgent) (42). RBD-specific V<sub>H</sub>H antibodies were affinity isolated and subsequently eluted by either increasing stringency of high pH buffer or salt. All the eluted V<sub>H</sub>Hs were neutralized and dialyzed into 1x DPBS before the quantitative proteomics analysis. RBD-specific V<sub>H</sub>H antibodies were reduced, alkylated and in-solution digested using either trypsin or chymotrypsin (27). After proteolysis, the peptide mixtures were desalted by self-packed stage-tips or Sep-Pak C18 columns (Waters) and analyzed with a nano-LC 1200 that is coupled online with a Q Exactive™ HF-X Hybrid Quadrupole Orbitrap™ mass spectrometer (Thermo Fisher). Proteomic analysis was performed as previously described and by using the Augur Llama- a dedicated software that we developed to facilitate reliable identification, label-free quantification, and classification of high-affinity Nbs (27). This analysis led to thousands of RBD-specific, high-affinity Nb candidates that belong to ~ 350 unique CDR3 families. From these, we selected 109 Nb sequences with unique CDR3s for DNA synthesis and characterizations.

#### *Nb DNA synthesis and cloning*

The monomeric Nb genes and the homotrimeric Nbs20 and 21 with the (GGGS)<sub>5</sub> linkers were codon-optimized and synthesized (Synbio). Nb DNA sequences were cloned into a pET-21b(+) vector or pET-22b(+) vector using EcoRI and HindIII or BamHI and XhoI restriction sites. To produce a heterodimeric Nb such as Nb21- Nb34, the DNA fragment of the monomeric Nb34 was first PCR amplified from the pET-21b(+) vector to introduce a linker sequence and two restriction sites of XhoI and HindIII that facilitate cloning. The PCR fragment was then inserted into the Nb21 pET-21b(+)vector to produce the heterodimer Nb21-(GGGS)<sub>2</sub>-Nb34. Homodimers or homotrimers with the EK linker were produced in-house. For the in-house generated constructs, a flexible linker sequence of EGKSSGSGSESKSTGGGGSEGKSSGSGSESKST introduced using the following two oligos:

CCGCTCGAGTGCTGCGGCCGCGGTGCTTTTGCTTTTCGCCGCTACCGCTGCTTTTACCTTCGCTGCCACC,  
and  
CCCAAGCTTGAAGGTAAAAGCAGCGGTAGCGGCGAAAGCAAAGCACCGGTGGCGGTGGCAGCGAAGG  
T ( Integrated DNA Technologies).

Briefly, after digestion using XhoI/HindIII restriction sites, the linker was inserted into pET21b(+)\_Nb21 or pET21b(+)\_Nb20 vector. For simplicity, here we used the Nb21 trimer for illustration of the cloning strategy. To shuffle the second copy of an Nb, we amplified Nb 21 from the pET21b(+) vector and introduced XhoI/NotI restriction sites. After digestion, the XhoI/NotI Nb fragment was inserted into the Nb\_linker vector to produce an Nb homodimer. The following DNA oligos were used to facilitate the cloning of the second copy of the linker in which EcoRI and BamHI sites were introduced:

CCGGAATTCGAGGTGCTTTTGCTTTTCGCCGCTACCGCTGCTTTTACCTTCGCTGCCACCGCCACCGGTGC  
,  
and  
CGCGGATCCGGTTCGAGCTCGGAAGGTAAAAGCAGCGGTAGCGGCGAAAGCAAAGCACCGGTGGCG  
G (Integrated DNA Technologies).

After digestion, the second linker was then inserted into the homodimeric pET21b(+)\_Nb21 vector. The third copy of the Nb21 gene was PCR amplified from the vector and inserted into the homodimeric pET21b(+)\_Nb21 construct using BamHI/SacI sites. All the DNA constructs were verified by sanger sequencing.

#### *Expression and purification of proteins*

Nb DNA constructs were transformed into BL21(DE3) cells and plated on Agar with 50 µg/ml ampicillin at 37 °C overnight. Cells were cultured in an LB broth to reach an O.D. of ~ 0.5- 0.6 before IPTG (0.5 mM) induction at 16°C overnight. Cells were then harvested, sonicated, and lysed on ice with a lysis buffer (1xPBS, 150 mM NaCl, 0.2% TX-100 with protease inhibitor). After cell lysis, protein extracts were collected by centrifugation at 15,000 X g for 10 mins and the his-tagged Nbs were purified by Cobalt resin and natively eluted by imidazole buffer (Thermo). Eluted Nbs were subsequently dialyzed in a dialysis buffer (e.g., 1x DPBS, pH 7.4). For periplasmic preparation of Nbs, cell pellets were resuspended in the TES buffer (0.1M Tris-HCl, pH 8.0; 0.25mM EDTA, pH 8.0; 0.25M Sucrose) and incubated on ice for 30 min. The supernatants were collected by centrifugation and subsequently dialyzed to DPBS. The resulting Nbs were then purified by Cobalt resin as described above.

The RBD (residues 319-541) of the SARS-Cov-2 spike (S) protein was expressed as a secreted protein in *Spodoptera frugiperda* Sf9 cells (Expression Systems) using the Bac-to-bac baculovirus method (Invitrogen). To facilitate protein purification, a FLAG-tag and an 8 × His-tag were fused to its N terminus, and a tobacco etch virus (TEV) protease cleavage site was introduced between the His-tag and RBD. Cells were infected with baculovirus and incubated at 27 °C for 60 h before harvesting. The conditioned media was added with 20 mM Tris pH 7.5 and incubated at RT for 1 h in the presence of 1 mM NiSO<sub>4</sub> and 5mM CaCl<sub>2</sub>. The supernatant was collected by centrifugation at 25,000 g for 30 min and then incubated with Nickel-NTA agarose resin (Clontech) overnight at 4 °C. After washing with buffer containing 20 mM Hepes pH 7.5, 200 mM NaCl, and 50mM imidazole, the RBD protein was eluted with the same buffer containing 400 mM Imidazole. Eluted protein was treated by TEV protease overnight to remove extra tags and further purified by size exclusion chromatography using the Superdex 75 column (Fisher) with a buffer containing 20 mM Hepes pH 7.5 and 150 mM NaCl. To obtain RBD and Nb20 complex, purified RBD was mixed with purified Nb20 in a molar ratio of 1: 1.5 and then incubated on ice for 2 hours. The complex was further purified using the Superdex 75 column with a buffer containing 20 mM Hepes pH 7.5 and 150 mM NaCl. Purified RBD-Nb20 complex was concentrated to 10-15 mg/ml for crystallization.

#### *ELISA (Enzyme-linked immunosorbent assay)*

Indirect ELISA was carried out to measure the relative affinities of Nbs. RBD was coated onto a 96-well ELISA plate (R&D system) at two ng/well in coating buffer (15 mM sodium carbonate, 35 mM sodium bicarbonate, pH 9.6) overnight at 4°C and was blocked with a blocking buffer (DPBS, 0.05% Tween 20, 5% milk) at room temperature for 2 hrs. Nbs were serially 10X diluted in the blocking buffer, starting from 1 µM to 0.1 pM, and 100 µl of each concentration was incubated with RBD-coated plates for 2 hrs. HRP-conjugated secondary antibodies against T7-tag (Thermo) were diluted 1:7500 and incubated with the well for 1 hr at room temperature. After PBST (DPBS, 0.05% Tween 20) washes, the samples were further incubated under dark with freshly prepared w3,3',5,5'-Tetramethylbenzidine (TMB) substrate for 10 mins to develop the signals. After the STOP solution (R&D system), the plates were read at multiple wavelengths (the optical density at 550 nm wavelength subtracted from the density at 450 nm) on a plate reader (Multiskan GO, Thermo Fisher). A non-binder was defined if any of the following two criteria were met: i) The ELISA signal was under detected at one µM concentration. ii ) The ELISA signal could only be detected at a concentration of 1 µM and was under detected at 0.1 µM concentration. The raw data was processed by Prism 7 (GraphPad) to fit into a 4PL curve and to calculate logIC<sub>50</sub>.

#### *Pseudotyped SARS-CoV-2 neutralization assay*

The 293T-hsACE2 stable cell line (Cat# C-HA101) and the pseudotyped SARS-CoV-2 virus particles with GFP (Cat# RVP-701G, Lot#CG-113A) or firefly luciferase (Cat# RVP-701L, Lot# CL109A, and CL-114A) reporters were purchased from the Integral Molecular. The neutralization assay was carried out according to the manufacturers' protocols. In brief, 10-fold serially diluted Nbs were incubated with the pseudotyped SARS-CoV-2-GFP for 1 hr at 37 °C for screening, while 3- or 5-fold serially diluted Nbs / immunized serum / immunized V<sub>H</sub>H mixture was incubated with the pseudotyped SARS-CoV-2-luciferase for accurate measurements. At least eight concentrations were tested for each Nb. Pseudovirus in culture media without Nbs was used as a negative control. The mixtures were then incubated with 293T-hsACE2 cells at 2.5x10<sup>5</sup> cells/ml in the 96-well plates. The infection took ~72 hrs at 37 °C with 5% CO<sub>2</sub>. The GFP signals (ex488/em530) were read using the Tecan Spark 20M with auto-optimal settings, while the luciferase signal was measured using the *Renilla*-Glo luciferase assay system (Promega, Cat# E2720) with the luminometer at 1 ms integration time. The obtained relative fluorescent/luminescence signals (RFU/RLU) from the negative control wells were normalized and used to calculate neutralization % for each concentration. For SARS-CoV-2-GFP screening, the 49 tested Nbs were divided into 6 groups based on their lowest tested concentration of 100% neutralization. For SARS-CoV-2-luciferase, data was processed by Prism7 (GraphPad) to fit into a 4PL curve and to calculate the logIC<sub>50</sub> ( half-maximal inhibitory concentration).

#### *Authentic SARS-CoV-2 plaque reduction neutralization test (PRNT)*

Nbs were diluted in a 2- or 3-fold series in Opti-MEM (Thermofisher). Each Nb dilution (110 µl) was mixed with 110 µl of SARS-CoV2Munich containing 100 plaque-forming units (p.f.u.) of the virus in Opti-MEM. The serum-virus mixes (220 µl total) were incubated at 37 °C for 1 h, after which they were added dropwise onto confluent Vero E6 cell monolayers in the six-well plates. After incubation at 37 °C, 5 % (v/v) CO<sub>2</sub> for 1 h, 2 ml of 0.1 % (w/v) immunodiffusion agarose (MP Biomedicals) in Dulbecco's modified eagle medium (DMEM) (Thermofisher) with 10 % (v/v) FBS and 1× pen-strep was added to each well. The cells were incubated at 37 °C, 5 % CO<sub>2</sub> for 72 h. The agarose overlay was removed and the cell monolayer was fixed with 1 ml/well formaldehyde (Fisher) for 20 min at room temperature. Fixative was discarded and 1 ml/well of 1 % (w/v) crystal violet in 10 % (v/v) methanol was added. Plates were incubated at room temperature for 20 min and rinsed thoroughly with water. Plaques were then enumerated and the 50 % plaque reduction neutralization titer (PRNT<sub>50</sub>) was calculated. A validated SARS- CoV-2 antibody-negative human serum control, a validated NIBSC SARS-CoV2 plasma control, was obtained from the National Institute for Biological Standards and Control, UK) and an uninfected cells control were also performed to ensure that virus neutralization by antibodies was specific.

#### *Surface plasmon resonance (SPR)*

Surface plasmon resonance (Biacore 3000, GE) was used to measure Nb affinities. Briefly, recombinant Nb was immobilized to the flow channels of an activated CM5 sensor-chip. Nb was diluted to 10 µg/ml in 10 mM sodium acetate, pH 5.5, and injected into the SPR system at 5 µl/min for 420 s. The surface was then blocked by 1 M ethanolamine-HCl (pH 8.5). For RBD analyte, a series of dilution (spanning ~ 1,000-fold concentration range) was injected in duplicate, with HBS-EP running buffer (GE-Healthcare) at a flow rate of 30 µl/min for 180 s, followed by a dissociation time of 20 mins. Between each injection, the sensor chip surface was regenerated twice with 6M Guanidine-HCl at a flow rate of 40-50 µl/min for 30 s - 1 min. Binding sensorgrams for each Nb were processed and analyzed using BIA evaluation by fitting with the 1:1 Langmuir model.

#### *Phylogenetic tree analysis and sequence logo*

Sequences were first aligned and numbered according to Martin's numbering scheme by ANARCI (43). The phylogenetic tree was constructed from aligned sequences by Molecular Evolutionary Genetics

Analysis(MEGA)(44) using the Maximum Likelihood method. The sequence logo was plotted from aligned sequences by logomaker(45).

#### *Epitope screening by size exclusion chromatography (SEC)*

Recombinant RBD and Nb proteins were mixed at a ratio of 1:1 (w:w) and incubated at 4°C for 1 hr. The complexes were analyzed by the SEC (Superdex75, GE LifeSciences) at a low rate of 0.4 ml/min for 1 hr using a running buffer of 20 mM HEPES, 150 mM NaCl, pH 7.4. Protein signals were detected by ultraviolet light absorbance at 280 nm.

#### *Chemical cross-linking and mass spectrometry (CXMS)*

Recombinant Nbs were first pre-incubated with the trypsin resin for approximately 2-5 mins to remove the N terminal T7 tag, which is highly reactive to the crosslinker. Nb was incubated with RBD in the pH 7.4 buffer at 4°C for 1 hr to allow the formation of the complex. The reconstituted complexes were then cross-linked with 2 mM disuccinimidyl suberate (DSS, ThermoFisher Scientific) for 25 min at 25°C with gentle agitation. The reaction was then quenched with 50 mM ammonium bicarbonate (ABC) for 10 min at room temperature. After protein reduction and alkylation, the cross-linked samples were separated by a 4–12% SDS-PAGE gel (NuPAGE, Thermo Fisher). The regions corresponding to the monomeric, cross-linked species (~45-50 kDa) were sliced and digested in-gel with trypsin and Lys-C (41, 46, 47). After efficient proteolysis, the cross-link peptide mixtures were desalted and analyzed with a nano-LC 1200 (Thermo Fisher) coupled to a Q Exactive™ HF-X Hybrid Quadrupole-Orbitrap™ mass spectrometer (Thermo Fisher). The cross-linked peptides were loaded onto a Picochip column (C18, 3 μm particle size, 300 Å pore size, 50 μm × 10.5 cm; New Objective) and eluted using a 60 min LC gradient: 5% B–10% B, 0 – 2 min; 10% B – 40% B, 2 – 50 min; 40% B–100% B, 50 – 60 min; mobile phase A consisted of 0.1% formic acid (FA), and mobile phase B consisted of 0.1% FA in 80% acetonitrile. The QE HF-X instrument was operated in the data-dependent mode. The top 4 most abundant ions (with the mass range of 350 to 2,000 and the charge state of +4 to +7) were fragmented by high-energy collisional dissociation (normalized HCD energy 30). The target resolution was 120,000 for MS and 15,000 for MS/MS analyses. The quadrupole isolation window was 1.6 Th and the maximum injection time for MS/MS was set at 300 ms. After the MS analysis, the data was searched by pLink for the identification of cross-linked peptides. The mass accuracy was specified as 10 and 20 p.p.m. for MS and MS/MS, respectively. Other search parameters included cysteine carbamidomethylation as a fixed modification and methionine oxidation as a variable modification. A maximum of three trypsin missed-cleavage sites was allowed. Initial search results were obtained using the default 5% false discovery rate, estimated using a target-decoy search strategy. The crosslink spectra were manually checked as previously described (46-49).

#### *Integrative structural modeling*

Structural models for Nbs were obtained using a multi-template comparative modeling protocol of MODELLER (50). Next, we refined the CDR3 loop (51) and selected the top 5 scoring loop conformations for the downstream docking in addition to 5 models from comparative modeling. Each Nb model was then docked to the RBD structure (PDB 6LZG) by an antibody-antigen docking protocol of PatchDock software that focuses the search to the CDRs and optimizes CXMS-based distance restraints satisfaction (52, 53). A restraint was considered satisfied if the Ca-Ca distance between two DSS cross-linked residues is within 28Å. The models were then re-scored by a potential statistical SOAP (54). The antigen interface residues (distance <6Å from Nb atoms) among the top 10 scoring models, according to the SOAP score, were used to determine the epitopes. The precision was estimated based on the convergence among the ten top-scoring models which was measured as the average RMSD between all the pairs.

#### *Crystallization, data collection, and structure determination of RBD-Nb20 complex*



Crystallization trials were performed with the Crystal Gryphon robot (Art Robbins). The RBD-Nb20 complex was crystallized using the sitting-drop vapor diffusion method at 17 °C. The crystals were obtained in conditions containing 100 mM sodium cacodylate pH 6.5 and 1 M sodium citrate. For data collection, the crystals were transferred to the reservoir solution supplemented with 20 % glycerol before freezing in liquid nitrogen. X-ray diffraction data were collected at the Advanced Photon Source (APS) beamline 23IDB of GM/CA with a 10µm-diameter microbeam. The data were processed using HKL2000 (55). Diffraction data from six crystals were merged to obtain a complete dataset with a resolution of 3.3 Å.

The structure was determined by the molecular replacement method in Phaser (56) using the crystal structures of RBD (PDB 6LZG) and an Nb (V<sub>H</sub>H-72, PDB 6WAQ) as search models. The initial model was refined in Phenix (57) and adjusted in COOT (58). The model quality was checked by MolProbity (59). The final refinement statistics were listed in Table S3.

Nb21 comparative modeling was done using the Nb20 structure as a template in MODELLER. All structure visualization figures were prepared using UCSF ChimeraX (60).

#### *Thermostability analysis of Nbs*

Nb thermostability was measured by differential scanning fluorimetry (DSF). To prepare DSF samples, Nbs were mixed with SYPRO orange dye (Invitrogen) in PBS to reach a final concentration of 12 µM. The samples were analyzed in triplicate using a 7900HT Fast Real-Time PCR System (Applied Biosystems) as previously described (41). The melting point was calculated by the first derivatives method (61).

#### *Nb stability test*

Nbs were dissolved in 20 mM HEPES, 150 mM NaCl, pH 7.5 at 0.4 mg/ml. 50% of the proteins were lyophilized by snap-freezing in liquid nitrogen, and speed-vac dried. ddH<sub>2</sub>O was used to reconstitute the proteins. The other 50% were aerosolized using a portable mesh atomizer nebulizer (MayLuck). The aerosolized droplets were collected in a microcentrifuge tube. SEC and pseudovirus neutralization assays were performed as described above to assess the properties and activities of the Nbs.

#### *Data availability*

The coordinates and structure factors for SARS-CoV-2 RBD with Nb20 have been deposited in the Protein Data Bank under the accession codes PDB 7JVB.

#### References

1. N. Zhu *et al.*, A Novel Coronavirus from Patients with Pneumonia in China, 2019. *N Engl J Med* **382**, 727-733 (2020).
2. P. Zhou *et al.*, A pneumonia outbreak associated with a new coronavirus of probable bat origin. *Nature* **579**, 270-273 (2020).
3. D. Wrapp *et al.*, Cryo-EM structure of the 2019-nCoV spike in the prefusion conformation. *Science* **367**, 1260-1263 (2020).
4. A. C. Walls *et al.*, Structure, Function, and Antigenicity of the SARS-CoV-2 Spike Glycoprotein. *Cell* **181**, 281-292 e286 (2020).
5. Y. Cai *et al.*, Distinct conformational states of SARS-CoV-2 spike protein. *Science*, (2020).
6. X. Fan, D. Cao, L. Kong, X. Zhang, Cryo-EM analysis of the post-fusion structure of the SARS-CoV spike glycoprotein. *Nat Commun* **11**, 3618 (2020).
7. Y. Cao *et al.*, Potent Neutralizing Antibodies against SARS-CoV-2 Identified by High-Throughput Single-Cell Sequencing of Convalescent Patients' B Cells. *Cell* **182**, 73-84 e16 (2020).
8. D. F. Robbiani *et al.*, Convergent antibody responses to SARS-CoV-2 in convalescent individuals. *Nature*, (2020).

9. J. Hansen *et al.*, Studies in humanized mice and convalescent humans yield a SARS-CoV-2 antibody cocktail. *Science*, (2020).
10. L. Liu *et al.*, Potent neutralizing antibodies against multiple epitopes on SARS-CoV-2 spike. *Nature*, (2020).
11. P. J. M. Brouwer *et al.*, Potent neutralizing antibodies from COVID-19 patients define multiple targets of vulnerability. *Science* **369**, 643-650 (2020).
12. D. Wrapp *et al.*, Structural Basis for Potent Neutralization of Betacoronaviruses by Single-Domain Camelid Antibodies. *Cell* **181**, 1436-1441 (2020).
13. A. Z. Wec *et al.*, Broad neutralization of SARS-related viruses by human monoclonal antibodies. *Science* **369**, 731-736 (2020).
14. T. Zohar, G. Alter, Dissecting antibody-mediated protection against SARS-CoV-2. *Nat Rev Immunol* **20**, 392-394 (2020).
15. N. Eroshenko *et al.*, Implications of antibody-dependent enhancement of infection for SARS-CoV-2 countermeasures. *Nat Biotechnol* **38**, 789-791 (2020).
16. S. Muyldermans, Nanobodies: Natural Single-Domain Antibodies. *Annu Rev Biochem* **82**, 775-797 (2013).
17. P. Vanlandschoot *et al.*, Nanobodies(R): new ammunition to battle viruses. *Antiviral Res* **92**, 389-407 (2011).
18. L. Detalle *et al.*, Generation and Characterization of ALX-0171, a Potent Novel Therapeutic Nanobody for the Treatment of Respiratory Syncytial Virus Infection. *Antimicrob Agents Chemother* **60**, 6-13 (2016).
19. R. A. Weiss, C. T. Verrips, Nanobodies that Neutralize HIV. *Vaccines-Basel* **7**, (2019).
20. I. Rossey *et al.*, Potent single-domain antibodies that arrest respiratory syncytial virus fusion protein in its prefusion state. *Nature Communications* **8**, (2017).
21. M. Schoof *et al.*, An ultra-potent synthetic nanobody neutralizes SARS-CoV-2 by locking Spike into an inactive conformation. *bioRxiv*, 2020.2008.2008.238469 (2020).
22. R. Konwarh, Nanobodies: Prospects of Expanding the Gamut of Neutralizing Antibodies Against the Novel Coronavirus, SARS-CoV-2. *Front Immunol* **11**, 1531 (2020).
23. T. F. Custódio *et al.*, Selection, biophysical and structural analysis of synthetic nanobodies that effectively neutralize SARS-CoV-2. *bioRxiv*, 2020.2006.2023.165415 (2020).
24. C. Liu *et al.*, Viral Architecture of SARS-CoV-2 with Post-Fusion Spike Revealed by Cryo-EM. *bioRxiv*, 2020.2003.2002.972927 (2020).
25. J. Gai *et al.*, A potent neutralizing nanobody against SARS-CoV-2 with inhaled delivery potential. *bioRxiv*, 2020.2008.2009.242867 (2020).
26. C. O. Barnes *et al.*, Structures of Human Antibodies Bound to SARS-CoV-2 Spike Reveal Common Epitopes and Recurrent Features of Antibodies. *Cell*, (2020).
27. Y. Xiang *et al.*, Integrative proteomics reveals exceptional diversity and versatility of mammalian humoral immunity. *bioRxiv*, 2020.2008.2021.261917 (2020).
28. M. P. Rout, A. Sali, Principles for Integrative Structural Biology Studies. *Cell* **177**, 1384-1403 (2019).
29. C. Yu *et al.*, Charting protein-protein interactions using Cross-Linking Mass Spectrometry (XL-MS). *Abstr Pap Am Chem S* **253**, (2017).
30. A. Leitner, M. Faini, F. Stengel, R. Aebersold, Crosslinking and Mass Spectrometry: An Integrated Technology to Understand the Structure and Function of Molecular Machines. *Trends Biochem Sci* **41**, 20-32 (2016).
31. B. T. Chait, M. Cadene, P. D. Olinares, M. P. Rout, Y. Shi, Revealing Higher Order Protein Structure Using Mass Spectrometry. *J Am Soc Mass Spectr* **27**, 952-965 (2016).
32. Q. H. Wang *et al.*, Structural and Functional Basis of SARS-CoV-2 Entry by Using Human ACE2. *Cell* **181**, 894+ (2020).
33. T. Li *et al.*, Potent synthetic nanobodies against SARS-CoV-2 and molecular basis for neutralization. *bioRxiv*, 2020.2006.2009.143438 (2020).
34. J. D. Walter *et al.*, Sybodies targeting the SARS-CoV-2 receptor-binding domain. *bioRxiv*, 2020.2004.2016.045419 (2020).
35. J. Huo *et al.*, Neutralizing nanobodies bind SARS-CoV-2 spike RBD and block interaction with ACE2. *Nat Struct Mol Biol*, (2020).

36. Y. L. Shu, J. McCauley, GISAID: Global initiative on sharing all influenza data - from vision to reality. *Eurosurveillance* **22**, 2-4 (2017).
37. A. Baum *et al.*, Antibody cocktail to SARS-CoV-2 spike protein prevents rapid mutational escape seen with individual antibodies. *Science* **369**, 1014-1018 (2020).
38. Y. Bar-On *et al.*, Safety and antiviral activity of combination HIV-1 broadly neutralizing antibodies in viremic individuals. *Nat Med* **24**, 1701-1707 (2018).
39. M. Marovich, J. R. Mascola, M. S. Cohen, Monoclonal Antibodies for Prevention and Treatment of COVID-19. *JAMA*, (2020).
40. I. Jovcevska, S. Muyldermans, The Therapeutic Potential of Nanobodies. *BioDrugs* **34**, 11-26 (2020).
41. Z. Shen *et al.*, A robust and versatile nanobody platform for drug delivery. *bioRxiv*, 2020.2008.2019.257725 (2020).
42. P. C. Fridy *et al.*, A robust pipeline for rapid production of versatile nanobody repertoires. *Nat Methods* **11**, 1253-1260 (2014).
43. J. Dunbar, C. M. Deane, ANARCI: antigen receptor numbering and receptor classification. *Bioinformatics* **32**, 298-300 (2016).
44. S. Kumar, G. Stecher, M. Li, C. Knyaz, K. Tamura, MEGA X: Molecular Evolutionary Genetics Analysis across Computing Platforms. *Mol Biol Evol* **35**, 1547-1549 (2018).
45. A. Tareen, J. B. Kinney, Logomaker: beautiful sequence logos in Python. *Bioinformatics* **36**, 2272-2274 (2020).
46. Y. Shi *et al.*, Structural characterization by cross-linking reveals the detailed architecture of a coatomer-related heptameric module from the nuclear pore complex. *Mol Cell Proteomics* **13**, 2927-2943 (2014).
47. Y. Shi *et al.*, A strategy for dissecting the architectures of native macromolecular assemblies. *Nat Methods* **12**, 1135-1138 (2015).
48. Y. Xiang, Z. Shen, Y. Shi, Chemical Cross-Linking and Mass Spectrometric Analysis of the Endogenous Yeast Exosome Complexes. *Methods Mol Biol* **2062**, 383-400 (2020).
49. S. J. Kim *et al.*, Integrative structure and functional anatomy of a nuclear pore complex. *Nature* **555**, 475-482 (2018).
50. A. Sali, T. L. Blundell, Comparative protein modelling by satisfaction of spatial restraints. *J Mol Biol* **234**, 779-815 (1993).
51. A. Fiser, A. Sali, ModLoop: automated modeling of loops in protein structures. *Bioinformatics* **19**, 2500-2501 (2003).
52. D. Schneidman-Duhovny *et al.*, A method for integrative structure determination of protein-protein complexes. *Bioinformatics* **28**, 3282-3289 (2012).
53. D. Schneidman-Duhovny, H. J. Wolfson, Modeling of Multimolecular Complexes. *Methods Mol Biol* **2112**, 163-174 (2020).
54. G. Q. Dong, H. Fan, D. Schneidman-Duhovny, B. Webb, A. Sali, Optimized atomic statistical potentials: assessment of protein interfaces and loops. *Bioinformatics* **29**, 3158-3166 (2013).
55. Z. Otwinowski, W. Minor, Processing of X-ray diffraction data collected in oscillation mode. *Methods Enzymol* **276**, 307-326 (1997).
56. A. J. McCoy *et al.*, Phaser crystallographic software. *J Appl Crystallogr* **40**, 658-674 (2007).
57. P. D. Adams *et al.*, PHENIX: a comprehensive Python-based system for macromolecular structure solution. *Acta Crystallogr D Biol Crystallogr* **66**, 213-221 (2010).
58. P. Emsley, K. Cowtan, Coot: model-building tools for molecular graphics. *Acta Crystallogr D Biol Crystallogr* **60**, 2126-2132 (2004).
59. C. J. Williams *et al.*, MolProbity: More and better reference data for improved all-atom structure validation. *Protein Sci* **27**, 293-315 (2018).
60. T. D. Goddard *et al.*, UCSF ChimeraX: Meeting modern challenges in visualization and analysis. *Protein Sci* **27**, 14-25 (2018).
61. F. H. Niesen, H. Berglund, M. Vedadi, The use of differential scanning fluorimetry to detect ligand interactions that promote protein stability. *Nat Protoc* **2**, 2212-2221 (2007).